

A QUANTITATIVE MANGANESE-ENHANCED MRI
METHOD FOR IN VIVO ASSESSEMENT OF
L-TYPE CALCIUM CHANNEL ACTIVITY IN HEART

by

WEN LI

Submitted in partial fulfillment of the requirements

For the degree of Doctor of Philosophy

Dissertation Adviser: Xin Yu, Sc.D.

Department of Biomedical Engineering

CASE WESTERN RESERVE UNIVERSITY

May 2011

CASE WESTERN RESERVE UNIVERSITY
SCHOOL OF GRADUATE STUDIES

We hereby approve the thesis/dissertation of

candidate for the _____ degree *.

(signed) _____

(chair of the committee)

(date) _____

*We also certify that written approval has been obtained for any proprietary material contained therein.

Dedication

To my parents, my wife and my daughter

Table of Contents

| | |
|---|----|
| Table of Contents | 1 |
| List of Figures | 4 |
| Acknowledgements | 8 |
| Lists of Symbols and Abbreviations | 10 |
| Abstract | 11 |
| Chapter 1 Introduction | 13 |
| 1.1 Excitation-Contraction Coupling and Calcium (Ca^{2+}) Cycling | 13 |
| 1.2 Manganese-Enhanced MRI | 14 |
| 1.2.1 Mn^{2+} – A Potent MRI Contrast Agent | 15 |
| 1.2.2 MEMRI – <i>In Vivo</i> Probe of Ca^{2+} Influx Rate | 16 |
| 1.3 Kinetic Modeling of Ca^{2+} Cycling using Quantitative MEMRI Measurement | 17 |
| 1.4 Objectives and Significances | 18 |
| Chapter 2 Evaluation of the Sensitivity of <i>In Vivo</i> MEMRI to Subtle Alterations in L-type Ca^{2+} Channel Activity | 21 |
| 2.1 Introduction | 21 |
| 2.2 Methods | 22 |
| 2.2.1 Animal Breeding | 22 |
| 2.2.2 Animal Preparation and MnCl_2 Infusion Protocol | 23 |
| 2.2.3 MRI Study | 24 |
| 2.2.4 Image Processing | 24 |
| 2.2.5 Statistical Analysis | 25 |
| 2.3 Results | 25 |

| | | |
|---|---|----|
| 2.3.1 | Animal Characteristics and Cardiac Function | 25 |
| 2.3.2 | Dynamics of Contrast Enhancement..... | 26 |
| 2.4 | Discussion | 27 |
| Chapter 3 A Fast T ₁ Mapping Method for Dynamic Quantification of Mn ²⁺ Accumulation in | | |
| Blood and Myocardium | | |
| 3.1 | Evaluation of Relaxivity under Different Physiological Conditions | 30 |
| 3.1.1 | Introduction | 30 |
| 3.1.2 | Methods | 31 |
| 3.1.3 | Results | 32 |
| 3.2 | SRLI for Fast T ₁ Mapping of Myocardium..... | 32 |
| 3.2.1 | Introduction..... | 32 |
| 3.2.2 | Methods..... | 34 |
| 3.2.3 | Results..... | 39 |
| 3.2.4 | Discussion..... | 44 |
| 3.3 | SRLI for Rapid Quantification of Arterial Input Function (AIF) | 48 |
| 3.3.1 | Introduction..... | 48 |
| 3.3.2 | Methods..... | 50 |
| 3.3.3 | Results..... | 52 |
| 3.3.4 | Discussion..... | 54 |
| Chapter 4 A Model-Based Compressed Sensing Method for Fast T ₁ mapping..... | | |
| 4.1 | Introduction | 58 |
| 4.2 | Methods..... | 60 |
| 4.2.1 | Model-Based Compressed Sensing..... | 60 |

| | | |
|--|--|----|
| 4.2.2 | Simulation Studies | 62 |
| 4.2.3 | Phantom Study | 63 |
| 4.2.4 | <i>In Vivo</i> Studies | 65 |
| 4.2.5 | Statistic Analysis..... | 66 |
| 4.3 | Results | 67 |
| 4.3.1 | Simulation Studies | 67 |
| 4.3.2 | Phantom Studies..... | 69 |
| 4.3.3 | <i>In Vivo</i> Studies | 70 |
| 4.4 | Discussion | 73 |
| Chapter 5 A Two-Compartment Kinetic Model for Quantification of Ca ²⁺ Cycling | | 78 |
| 5.1 | Introduction | 78 |
| 5.2 | Methods..... | 79 |
| 5.2.1 | Two-Compartment Kinetic Model..... | 79 |
| 5.2.2 | Perfusion MEMRI Experiment..... | 80 |
| 5.2.3 | Model Validation | 82 |
| 5.3 | Results and Conclusion | 82 |
| Chapter 6 Conclusion and Future Directions..... | | 84 |
| 6.1 | Conclusion..... | 84 |
| 6.2 | Future Directions..... | 85 |
| 6.2.1 | Evaluation of Ca ²⁺ Efflux Rate with MEMRI..... | 85 |
| 6.2.2 | Development of Standardized DCE-MRI..... | 85 |
| 6.2.3 | Translating MEMRI Method to Clinical Practices | 86 |
| Bibliography | | 88 |

List of Figures

| | |
|--|----|
| Figure 1.1 Ca^{2+} cycling in myocyte. <i>From Bers, Nature 2002;415:198</i> | 14 |
| Figure 2.1 (a) Heart rate of the control and $\text{adbn}^{(-/-)}$ mice during the 30-min Mn^{2+} infusion and 30-min post-injection period; (b) Ejection fraction at baseline and at the end of post-contrast period. (Error bars = 1 SD.) | 26 |
| Figure 2.2 (a) Representative T_1 -weighted short-axis images acquired during Mn^{2+} protocol; (b) Time course of signal enhancement of the control and $\text{adbn}^{(-/-)}$ mice; (c) The percentage | 27 |
| Figure 3.1 Relaxivity of MnCl_2 at different albumin and Ca^{2+} concentrations. | 32 |
| Figure 3.2 SRTL pulse sequence. An ECG-triggered saturation module is followed by N successive ECG-triggered FLASH acquisitions. | 35 |
| Figure 3.3 Simulation of the effect of TR on T_1 estimation. a-d. Fitted T_1 versus theoretical T_1 . The error bar is the standard deviation from 25 simulations. e-h. Bland-Altman plots of the difference between fitted T_1 and theoretical T_1 . The middle dotted line is the mean of the difference. The upper and bottom dotted lines are the mean plus and minus two times of the standard deviation, respectively. | 40 |
| Figure 3.4 Simulation of the effect of τ fluctuation on T_1 estimation with TR = 2.4 s and $\tau = 0.24$ s. a-c. Fitted T_1 versus theoretical T_1 . The error bar is the standard deviation from 25 simulation runs. d-f. Bland-Altman plots of the difference between fitted T_1 and theoretical T_1 . The middle dotted line is the mean of the difference. The upper and bottom dotted lines are the mean plus and minus two times of the standard deviation, respectively. | 41 |
| Figure 3.5 Simulation of the estimation errors caused by beat-to-beat variations in rotational and translational motion. a. Digital phantom with four segments of different, representative T_1 values. b-d. Estimated T_1 maps with random translational motion (b), | |

rotational motion (c), and both rotational and translational motion (d) incorporated, respectively. e-g. Difference maps between theoretical and fitted T_1 maps (b-d), respectively.

..... 42

Figure 3.6 Phantom study. a&b. T_1 -weighted image and T_1 map of the phantom tubes, respectively. Phantoms 1 to 8 contained $MnCl_2$ solutions with the following concentrations (in mM): 1000, 900, 700, 500, 300, 200, 100, and 30. c. Longitudinal relaxation rate constant (R_1) versus Mn^{2+} concentration. d. T_1 values measured with different flip angles. The horizontal lines are the T_1 values measured by the standard SR method. 44

Figure 3.7 In vivo T_1 mapping. a-c. T_1 -weighted images acquired at 2τ , 4τ , and 10τ after the saturation pulses, respectively. d. Mean T_1 values of the LV myocardium measured by SRTL and standard inversion recovery Look-Locker (IRLL) method before and after Mn^{2+} injection. e. Bland-Altman plot comparing T_1 values measured by SRTL method and IRLL method. . 45

Figure 3.8 R_1 changes in dynamic MEMRI study. a&b. Representative T_1 maps of a heart pre- and post- $MnCl_2$ injection, respectively. c. Time course of R_1 changes tracked by SRTL at a temporal resolution of 3 min. 46

Figure 3.9 (a)&(b) Signal intensity profile along the long axis of the cylindrical water phantom. Partial-body and whole-body saturation was achieved by the mouse coil (a) and rat coil (b), respectively. (c) Normalized signal intensity (SI) evolution of the left ventricular blood after saturation preparation in mouse..... 53

Figure 3.10 (a) Time courses of blood and myocardium R_1 in response to Mn^{2+} injection; (b) – (d) R_1 maps acquired at baseline (b), end of 30 min infusion (c) and end of 30 min washout period (d)..... 54

Figure 3.11 Changes in ΔR_1 and absolute Mn^{2+} concentration at the end of injection and washout sessions. 55

Figure 4.1 CS reconstruction of the Shepp-Logan phantom images simulated with different acceleration factors, R. (a) Reconstructed T_1 weighted images at $t = 1.5$ s after saturation preparation; (b) The resulting T_1 maps; (c) Difference maps between the reconstructed and the theoretical T_1 maps. The NRMSE is presented at the bottom of each image/map. The direction of phase encoding is from left to right. 67

Figure 4.2 CS reconstructed T_1 maps at different spatial resolution. Acceleration factors of 2, 4 and 8 were employed to under-sample k-space images with a matrix size of (a) 128x128; (b) 256x256, and (c) 512x512, respectively. The NRMSE is presented at the bottom of each T_1 map. The direction of phase encoding is from left to right. 68

Figure 4.3 The impact of SNR and high spatial-frequency structures on CS reconstruction. (a) The NRMSE of the reconstructed T_1 maps at different SNR; (b) Theoretical T_1 map showing focal regions with different pixel numbers; (c)-(e) Pixel-wise differences between the theoretical and CS estimated T_1 values in the regions outlined in (b). 70

Figure 4.4 Impact of using phase maps for CS reconstruction. The direction of phase encoding is from left to right. (a)-(d) Reconstructed T_1 maps without using a pre-calculated phase map (a) and using the phase maps calculated from the 8 center PE lines (b), the fully sampled M_0 image (c) , and a separate fully sampled T_1 mapping dataset (d), respectively. The NRMSE is presented at the bottom of each T_1 map. (e)-(h) Corresponding difference images of the fully sampled and CS reconstructed T_1 maps. 71

Figure 4.5 Phase map of the *in vivo* mouse heart. (a) Phase map of the M_0 image. (b) Absolute difference in phase values between the M_0 image and a SPLL image acquired at

baseline. (c)&(d) Phase values of the M_0 image versus phase values of (c) all SRL images acquired at baseline and (d) every ninth SRL images in the T_1 datasets acquired during the entire MEMRI period..... 72

Figure 4.6 *In vivo* MEMRI study of the mouse heart. (a) T_1 weighted image acquired with full sampling at 1.5 s after saturation preparation; (b) reconstructed under-sampled image using zero-padding; (c) CS reconstructed under-sampled image; (d)-(f) The corresponding T_1 maps; (g)&(h) The corresponding differences maps of T_1 ; (i)&(j) Bland–Altman plots showing the difference in T_1 values estimated from the fully-sampled dataset and under-sampled dataset (i) or CS reconstructed dataset (j); (k) Time courses of the average myocardial T_1 values during the contrast infusion period. The direction of phase encoding is from left to right. Yellow arrows indicate the aliasing artifact. 74

Figure 5.1 Two compartment model to describe Mn^{2+} dynamics. 79

Figure 5.2 Sensitivity analysis of the MEMRI model. 83

Figure 5.3 Model fitted Mn^{2+} influx and efflux rates for the perfusion MEMRI datasets.... 83

Acknowledgements

The pursuit of my Ph.D. degree has been a long and memorable journey, paved with countless efforts, excitements and frustrations. Now to the end of it, I am filled with genuine appreciation for all the people that supported me along the way.

First and foremost, I would like to express my deepest gratitude to my adviser Dr. Xin Yu for her invaluable guidance, continuous and generous support through the years. Her broad expertise and sharp insight in the field of cardiovascular MR exposed me to a wide spectrum of excitements. Her passion in research and rigorous working attitude set a great model to follow. Her extraordinary mentoring helped me grow from a student to an independent researcher.

I am also very grateful for the enormous support and mentoring from my thesis committee. Dr. Chris Flask is not only a teacher who guided me in the MR field, but also a good friend who offered precious advices on how to cope with the ups and downs in research and life. Dr. Mark Griswold has a distinguished expertise and insight in fast imaging. His suggestions and inspirations were critically important for the development of fast T_1 mapping methods. Dr. David Rosenbaum provided invaluable suggestions from a physician's perspective, which made the physiological component of the project sound and significant. In addition, his advice on how to communicate with people from different fields has a significant impact on my career far beyond the Ph.D. years. I am also very thankful to Dr. David Wilson's thoughtful suggestions on the design of the project.

I owe my sincere appreciation to everybody in my lab and the Case Center for Imaging Research. I would like to extend a special thanks to Dr. Ming Lu for his help on the development of the kinetic model in the current thesis.

I am indebted to my family for their long term support and sacrifice. I want to thank my wife for her understanding of the countless nights and weekends I spent on work, for her continuous warm encouragements and selfless contributions to the family. I sincerely appreciate the spiritual, physical and financial supports from my parents and in-laws. They always believed in me about my decisions. I feel blessed to have my daughter Isabella join us in the midst of my Ph.D. study. The joys she brought were incomparable and were the greatest motivations to support me through the most difficult times.

This acknowledgement list can be expanded on and on. I will stop here and send my sincere regards and blessings to everyone who contributed to this thesis.

Lists of Symbols and Abbreviations

AAS – Atomic absorption spectroscopy

bpm – Beats per minute

Ca²⁺ – Divalent calcium ions

DCE – Dynamic contrast-enhanced

EPI – Echo planar imaging

FLASH – Fast low angle shot

Gd – Gadolinium

IRLL – Inversion recovery Look-Locker

LV – Left ventricle

M_z – Longitudinal magnetization

Mn²⁺ – Divalent manganese ions

MEMRI – Manganese-enhanced MRI

ROI – Region of interest

SAR – Specific absorption rate

SNR – Signal-to-noise ratio

SR – Saturation recovery

SRLI – Saturation recovery Look-Locker

SD – Standard deviation

WT – Wild-type

A Quantitative Manganese-Enhanced MRI Method for *In Vivo* Assessment of
L-type Calcium Channel Activity in Heart

Abstract

by

WEN LI

Ca^{2+} cycling between the cellular and subcellular compartments plays an important role in regulating cardiac contraction. Disturbance in Ca^{2+} handling occurs in heart failure and is closely related to abnormal contractile performance. The influx of extracellular Ca^{2+} through L-type calcium channel is the trigger and a key player in the Ca^{2+} cycling process. However, there are limited ways to measure it *in vivo*. Recently, manganese (Mn^{2+})-enhanced MRI (MEMRI) has been proposed as a promising probe to assess Ca^{2+} uptake because Mn^{2+} also enters the cell through the Ca^{2+} channels. However, quantitative analysis and substantial validation are still lacking, which has limited the application of MEMRI as an *in vivo* method for quantitative delineation of the Ca^{2+} influx rate.

In the current thesis project, a quantitative MEMRI method was developed and validated using small animal models. The sensitivity to subtle alterations in Ca^{2+} influx rate was demonstrated in a qualitative MEMRI study using a genetically manipulated mouse model that manifested slightly altered L-type Ca^{2+} channel activity. To provide quantitative estimation of Mn^{2+} dynamics, fast T_1 mapping techniques were developed based on the direct linear relationship between Mn^{2+} concentration and proton R_1 . An ECG-triggered saturation recovery Look-Locker (SRL) method and a model-based compressed sensing method was

developed and validated, respectively. When these two methods were combined, rapid T_1 mapping (< 80 s) of both myocardium and blood were achieved at high spatial resolution ($234 \times 469 \mu\text{m}^2$). Subsequently, a kinetic model was developed to determine Ca^{2+} influx rate from the quantitative MEMRI measurements. The robustness and accuracy of estimated Ca^{2+} influx rate was validated using perfusion MEMRI datasets with L-type Ca^{2+} channel activity well controlled by buffer ingredients.

In conclusion, the accomplishment of this project provides a robust MEMRI method for *in vivo* quantification of L-type Ca^{2+} channel activity in small animals. It can improve the diagnosis and treatment evaluation of diseases that involve abnormal Ca^{2+} influx rate, e.g., hypertension. The fast T_1 mapping methods developed in the current study can also be readily applied to other dynamic contrast enhanced MRI studies to provide quantitative estimation of contrast agent accumulation.

Chapter 1 Introduction

1.1 Excitation-Contraction Coupling and Calcium (Ca^{2+}) Cycling

Cardiac contraction plays a critical role in our life by pumping blood throughout the body. The mechanical contraction is mediated by a series of electrical stimulus, a physiological process often referred to as excitation-contraction (EC) coupling (1). Calcium ion (Ca^{2+}) cycling between various cellular and subcellular compartments is central to EC coupling (Fig. 1.1). Specifically, cardiac cycle is initiated by a flux of Ca^{2+} from extracellular space into cell through the voltage gated L-type Ca^{2+} channel. This Ca^{2+} entry stimulates a larger Ca^{2+} release from the sarcoplasmic reticulum through the ryanodine receptor, a process often referred to as Ca^{2+} -induced Ca^{2+} release. The resulting increase in cytosolic Ca^{2+} leads to the binding of Ca^{2+} to troponin C that induces cross-bridge cycling and muscle contraction. After the contraction, cytosolic Ca^{2+} is quickly cleared out to allow diastolic relaxation. The cellular uptake and removal of Ca^{2+} must be balanced to maintain Ca^{2+} homeostasis. Disturbance in Ca^{2+} handling may lead to altered cytosolic Ca^{2+} concentration, which are often related to the pathological performance of the heart (2, 3).

Currently, *in vivo* evaluation of Ca^{2+} cycling remains a challenge mainly because of the following reasons (4). First, the amount of Ca^{2+} which enters and leaves the cell is extremely small when compared to the amount of extracellular Ca^{2+} available. Second, the Ca^{2+} fluxes only occur for a very short amount of time. Currently, whole cell patch clamp technique allows *in vitro* assessment of Ca^{2+} fluxes in isolated cells (5). However, an established method for *in vivo* measurement is still lacking.

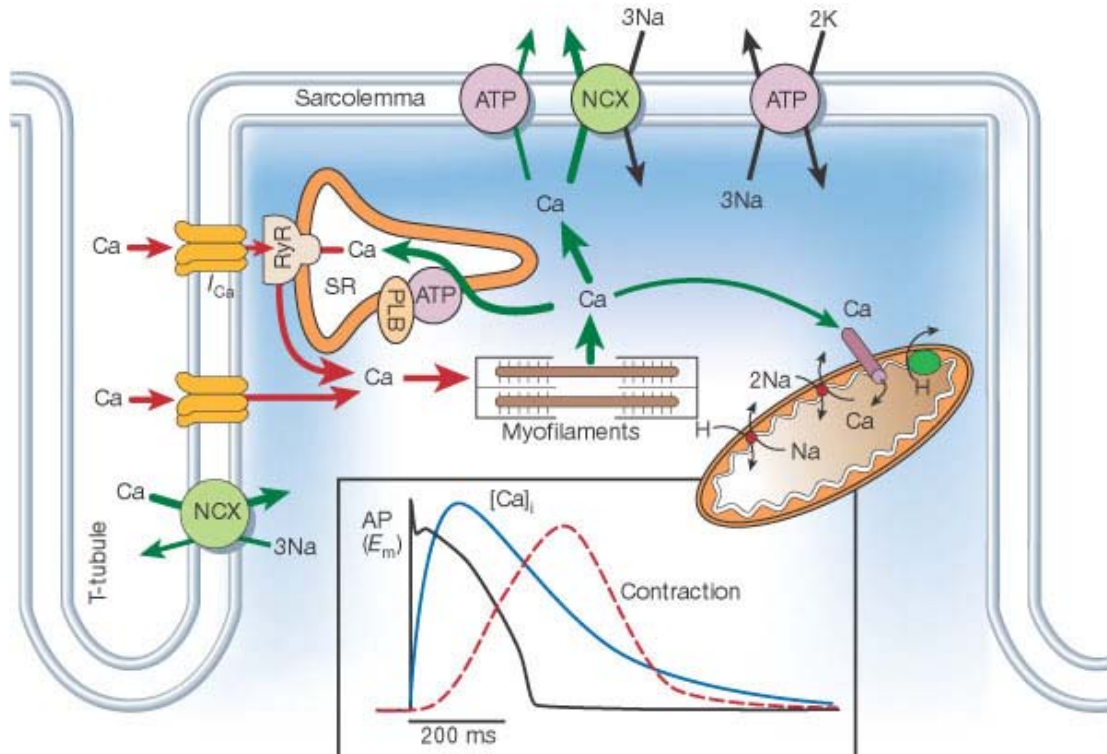


Figure 1.1 Ca^{2+} cycling in myocyte. *From Bers, Nature 2002;415:198*

1.2 Manganese-Enhanced MRI

Manganese ion (Mn^{2+}), a potent MRI contrast agent, has been suggested as a promising surrogate to evaluate Ca^{2+} cycling *in vivo* (4-7). Up to date, most manganese-enhanced MRI (MEMRI) studies focused on the evaluation of Ca^{2+} influx through the voltage-gated L-type Ca^{2+} channels because the influx rate of Mn^{2+} has a linear relationship to that of Ca^{2+} when low Mn^{2+} dose was injected (4, 8). Recently, MEMRI was also employed to study Ca^{2+} efflux through the sodium (Na^+)/ Ca^{2+} exchanger (7). However, complete elucidation of the Mn^{2+} efflux mechanism remains lacking, which limits the use of MEMRI for reliable estimation of Ca^{2+} efflux. Therefore, in the current project, we focused on the

development and validation of an *in vivo* MEMRI method to quantitatively delineate the influx rate of Ca^{2+} through the L-type Ca^{2+} channel.

1.2.1 Mn^{2+} – A Potent MRI Contrast Agent

As the first MRI contrast agent, Mn^{2+} was discovered by Paul Lauterbur in the 1970s (9). It is paramagnetic, with positive susceptibility and unpaired electron. The unpaired electron generates a strong local magnetic dipole moment that is normally three orders of magnitude larger than that of protons (10). This greatly increases the energy release rate (longitudinal relaxation time constant, T_1) of the surrounding excited water protons (11). The strong local field also increases the variations of the accumulated phases of surrounding water protons, which leads to reduced transverse relaxation time constant, T_2 .

In the early days, Mn^{2+} was used to study macromolecular structure with NMR via its binding to nucleic acids or proteins (12, 13). It was also used to quantify water exchange rate through the cell membrane (14). However, the toxicity of Mn^{2+} hindered its early development to *in vivo* studies, especially as T_2 contrast agent since it requires a high dose of Mn^{2+} . Recently, Mn^{2+} regains research interests as a T_1 contrast agent. The advancement in MRI technology now allows the detection of Mn^{2+} induced signal enhancements at a small dose that does not cause any noticeable side effects (15, 16).

Currently, MEMRI is primarily applied for the following uses. The first use is to trace specific neuronal connections in the brain (17-20). The second use is to enhance the contrast of brain images for better view of the structures (21, 22). The third use is to monitor Ca^{2+} channel activities since Mn^{2+} enters and leaves cell through the same channels as Ca^{2+} (4, 7).

1.2.2 MEMRI – *In Vivo* Probe of Ca²⁺ Influx Rate

The ability of MEMRI in probing Ca²⁺ channel activity stems from the analogue behavior of Mn²⁺ to Ca²⁺ in physiological system. Specifically, Mn²⁺ has very similar physical and chemical characteristics as Ca²⁺. The radius of Mn²⁺ (67 pm) is close to that of Ca²⁺ (100 pm) (23). The most stable forms of manganese and calcium are both divalent. Therefore, Mn²⁺ enters excitable cells via the same voltage gated L-type Ca²⁺ channels as Ca²⁺ (24). Once inside the cell, Mn²⁺ has a high affinity to the Ca²⁺ and Mg²⁺ binding sites on proteins and nucleic acids (25). Thus, the intracellular retention time of Mn²⁺ can be hours under *in vivo* condition (4). As such, the accumulation rate of intracellular Mn²⁺ can be measured to indirectly evaluate the activity of L-type Ca²⁺ channels (6, 26-29).

An important assumption of the above approach is that the influx rate of Mn²⁺ is linearly related to the activity of L-type Ca²⁺ channels. With a low injection dose of Mn²⁺, such assumption is satisfied in most current MEMRI studies. The extracellular concentration of Mn²⁺ (~ 30µM) (8, 30, 31) is significantly smaller than that of Ca²⁺ (~ mM) (32). Therefore, the disturbance from Mn²⁺ influx to L-type Ca²⁺ channel activity can be neglected.

Recently, MEMRI is increasingly used in research to study Ca²⁺ channel activities. Its safety and efficacy was thoroughly evaluated in both *ex vivo* and *in vivo* studies using rats (33), guinea pigs (34), mice (6) and human (8, 35). Apparent signal changes were observed with the use of Mn²⁺ doses that did not cause any neurological disorders or cardiac depressions. In addition, MEMRI exhibited a high sensitivity to Ca²⁺ influx alterations induced by inotropic states (36), ischemia (26) and myocardial infarction (37). However, these observations only provided qualitative estimations of the Ca²⁺ influx rate because the track of Mn²⁺ dynamics was based on T₁-weighted signal intensities. The T₁-weighted signal

intensities are inevitably affected by other sources that are hard to predict, i.e., inhomogeneous B_0/B_1 field and T_2 distribution. Therefore, only qualitative estimation of the Mn^{2+} distributions can be achieved (38). Alternatively, a direct measurement of T_1 , the intrinsic tissue characteristic, would provide quantitative MEMRI analysis that is independent of hardware imperfections and operation variations (38). However, T_1 mapping normally takes a long imaging time, which limits its application in MEMRI studies.

1.3 Kinetic Modeling of Ca^{2+} Cycling using Quantitative MEMRI Measurement

In dynamic contrast enhanced MRI (DCE-MRI) studies, kinetic models are frequently used to quantify the transfer rates of contrast agent between different cellular compartments. These models use mass-balance equations to describe the complex physiological processes that contrast agent undergoes. By fitting the model to experimentally acquired data of contrast agent dynamics, quantitative estimation of physiological parameters can be achieved such as blood vessel permeability, blood vessel volume fractions, and extracellular volume fractions (38, 39). The common assumption for such analysis is that the defined compartments in which contrast agent stays do not experience any characteristics change on the time scale of the DCE-MRI experiment. An additional assumption is that homogeneous distribution of the contrast agent within each compartment happens immediately after the contrast agent entering the compartment.

In DCE-MRI studies that employ gadolinium (Gd) as the contrast agent, the compartment model that contains intravascular and extracellular spaces is widely used (40-42). In MEMRI studies, a two-compartment model is needed since Mn^{2+} can also cross the cell membrane. The additional intracellular compartment increases the number of unknown

parameters and presents higher requirement on the accuracy of the experimental data. To date, only one MEMRI study has used such kinetic model to quantify the Ca^{2+} influx rate in human heart (8). However, the huge discrepancy between model fitted parameters and their corresponding physiological conditions degrades the reliability of the model. The inconsistency may originate from both unrealistic assumptions in the model and inaccurate estimation of the Mn^{2+} dynamics. Therefore, a two-compartment model with realistic constraints needs to be developed and validated for the estimation of Ca^{2+} influx rate.

1.4 Objectives and Significances

To sum up the above analysis, the following problems limit the establishment of a robust MEMRI method for quantitative assessment of cardiac Ca^{2+} influx rate. First, an accurate data acquisition technique is lacking. T_1 -weighted signal intensity can only provide qualitative estimation of Mn^{2+} concentration due to the lack of a direct relationship between signal enhancement and Mn^{2+} concentration. Second, a realistic two-compartment model is yet to be developed and validated. To address these challenges, the following specific aims were proposed to fulfill the current project.

1. *Validate the sensitivity of MEMRI to subtle alterations in Ca^{2+} influx at baseline state*

In vivo MEMRI characterization was performed on α -dystrobrevin knockout ($\text{adbn}^{-/-}$) mice and their wild-type (WT) littermates. MRI-observed changes in signal enhancement (T_1 -weighted images) was correlated with the changes in Ca^{2+} influx previously measured by *in vitro* patch clamp experiment. The positive results would broaden the application scope of

MEMRI method and magnify the significance of the following efforts to make the MEMRI method quantitative. Details are described in chapter 2.

2. *Establish a rapid T_1 mapping method to track Mn^{2+} dynamics in blood and myocardium*

Since Mn^{2+} concentration is linearly related to changes in relaxation rate (R_1), a fast T_1 ($1/R_1$) mapping technique was developed to track Mn^{2+} dynamics. The linear coefficient, also referred to as relaxivity (r_1), was evaluated in solutions with a wide range of albumin and Ca^{2+} concentrations to simulate potential physiological variations in MEMRI experiment.

An ECG-triggered saturation recovery Look-Locker (SRLL) method was developed for fast T_1 mapping of both blood and myocardium. Validation was conducted on both phantom and *in vivo* mouse hearts. Accuracy of the myocardial T_1 measurement was demonstrated by comparing the T_1 values measured by SRLL and the gold-standard inversions recovery Look-Locker (IRLL) method. Validation for measurement of blood T_1 was performed in a two-dose MEMRI experiment. The absolute Mn^{2+} concentration was measured by a chemical analysis method, atomic absorption spectroscopy (AAS). The accuracy of SRLL measured blood T_1 was demonstrated by its consistent linear relationships with AAS measured Mn^{2+} concentration in both dose groups.

The accomplishment of this aim would provide a solid quantitative data acquisition method not only for the current MEMRI study, but also for other DCE-MRI studies. Standardized DCE-MRI protocols can be developed to improve the objectiveness and accuracy of the analysis. Details are described in chapter 3.

3. *Develop a model-based compressed sensing method to expedite T_1 measurement*

A model-based compressed sensing (CS) method was developed to expedite T_1 mapping. Parameter optimization and reconstruction validation was performed on both simulated phantom and *in vivo* mouse heart. Reconstruction errors were quantified to assess the acceleration potential. The practical application was demonstrated in an *in vivo* MEMRI experiment.

The completion of the current study would provide faster T_1 acquisition, which allows more data points to be sampled during the Mn^{2+} enhancement period and therefore improves the accuracy of the subsequent kinetic analysis. Such gain can also be translated to increase the spatial resolution so uptake abnormalities at finer spots can be detected. Details are described in chapter 4.

4. *Develop a kinetic model to quantify Ca^{2+} influx rate*

A two-compartment model was developed to estimate Mn^{2+}/Ca^{2+} influx rate constant (k_i) based on the time course of myocardial and blood T_1 values. Validation was conducted on perfusion MEMRI datasets with well controlled Ca^{2+} influx rates. The model fitted k_i was correlated with the expected Ca^{2+} influx rates to validate the robustness of the modeling and MEMRI measurements.

The establishment of this kinetic model analysis would provide a quantitative estimation of Ca^{2+} influx rate and L-type Ca^{2+} channel activity that is free of the effects from Mn^{2+} in extracellular space and capillary. Other parameters such as efflux rate and extracellular volume fraction can also be quantified, providing supplementary diagnosis information. Details are described in chapter 5.

Chapter 2 Evaluation of the Sensitivity of *In Vivo* MEMRI to Subtle Alterations in L-type Ca²⁺ Channel Activity

2.1 Introduction

Excitation-contraction (EC) coupling, the process that converts electrical stimulus to muscle contraction, is the key regulator of cardiac function. Disturbance in Ca²⁺ handling occurs in heart failure and is closely related to abnormal contractile performance (2). The influx of extracellular Ca²⁺ through L-type calcium channel is the trigger and a key player in the Ca²⁺ cycling process. However, there are limited ways to evaluate the activity of L-type Ca²⁺ channel *in vivo*.

Manganese ion (Mn²⁺), a potent MRI contrast agent that enter the viable cells via the L-type Ca²⁺ channels, has been proposed as a potential Ca²⁺ surrogate to evaluate Ca²⁺ influx rate *in vivo* (4, 43). Despite of the analogue behavior in entering the cell, Mn²⁺ stays intracellular for hours (4, 7, 34) while Ca²⁺ redistributes between intra- and extracellular spaces in each heart beat. The long intracellular retention time of Mn²⁺ is mainly attributed to the lack of highly efficient exit routes and the strong binding to proteins and macromolecules (4, 34, 44). Because of its paramagnetic property, the accumulation of Mn²⁺ would increase the relaxation rate (R₁) of the surrounding water protons in a linear fashion over a wide range of concentration (8). Thus, a non-invasive quantification of the Mn²⁺ influx rate can be achieved by measuring either T₁ or T₁-weighted signal intensity. In addition, Mn²⁺ influx rate is approximately linear to the activity of the L-type Ca²⁺ channels when the extracellular concentration of free Mn²⁺ is significantly lower than the Michaelis-Menten constant of the Mn²⁺ for Ca²⁺ channels (45). Therefore, with an appropriate selection

of Mn^{2+} dose, manganese-enhanced MRI (MEMRI) offers a promising means to evaluate *in vivo* L-type Ca^{2+} channel activities by tracking Mn^{2+} -induced changes in relaxation.

The early development of MEMRI was hampered by the notion that overexposure to Mn^{2+} leads to cardiac failure as Mn^{2+} acts as a competitor to Ca^{2+} for the L-type calcium channels (46). However, experimental studies showed that depression of contractility requires a free extracellular Mn^{2+} concentration of 25 $\mu\text{mol/kg}$ (34, 47-49). With the advancement in MRI technology, significant signal changes were observed at Mn^{2+} doses that are far less than this in both animals (6, 33, 43) and human (8) studies. The Mn^{2+} -induced signal changes has been shown to be sensitive to alterations in Ca^{2+} influx rate associated with drug-induced inotropic states (6), ischemia (26), and myocardial infarction (29, 50). Recently, MacGowan et al also suggested that MEMRI can sensitize the changes of Ca^{2+} influx associated with altered protein components in a transgenic mouse model (51).

The goal of the current study is to explore the sensitivity of MEMRI to more subtle changes in Ca^{2+} channel activity. The α -dystrobrevin knockout ($adbn^{-/-}$) mice were used as the animal model since they exhibited a small increase in currents through the L-type Ca^{2+} channels in our previous whole cell patch clamp studies (52). In the current study, the *in vivo* MEMRI results were compared with the *in vitro* patch clamp measurements to demonstrate the sensitivity of MEMRI to subtle alterations in L-type Ca^{2+} channel activity.

2.2 Methods

2.2.1 Animal Breeding

The mouse colony was established by breeding the $adbn^{-/-}$ mice with WT C57BL/6 mice purchased from the Jackson Laboratory (Bar Harbor, ME). Heterozygous ($adbn^{+/-}$)

mice were used as the breeders to generate the mutants ($adbn^{-/-}$) and the WT littermates (controls). MEMRI studies were performed on 4 months old male $adbn^{-/-}$ mice (n=9) and their WT littermates (n=9) to explore the sensitivity of MEMRI to altered Ca^{2+} handling. All procedures were approved by the Institutional Animal Care and Use Committee of the Case Western Reserve University.

2.2.2 Animal Preparation and $MnCl_2$ Infusion Protocol

The animals were prepared as described previously (53). Briefly, mice were anesthetized with 1% isoflurane. A catheter was inserted into the abdomen for intraperitoneal infusion of $MnCl_2$. The animals were then moved into the magnet in prone position. Electrodes were attached to the front paw and left leg to obtain ECG signals. A water balloon was tightly taped on the top of the mouse back to monitor respiration. An anal temperature probe was inserted to record body temperature. All physiological signals were transferred through an optical fiber to a laptop for monitoring and recording (SA Instruments Inc., Stony Brook, NY). The animals were kept warm by blowing hot air into the magnet using a blow dryer. The heat flow and the anesthesia level were manually adjusted to maintain a heart rate around 500 bpm at baseline. A phantom tube filled with 20 μM $MnCl_2$ solution was placed adjacent to the mouse body to provide reference signal. During the imaging study, 126 mM $MnCl_2$ solution was infused at a constant rate of 0.2 ml/hr for 30 min with the aid of a syringe pump (Braintree Scientific Inc., MA), followed by a 30 min post-contrast period.

2.2.3 MRI Study

Imaging study was performed on a horizontal 9.4T Bruker Biospec scanner (Bruker Biospin Co. Billerica, MA) equipped with a 35-mm birdcage RF coil. A short-axis slice at the midventricular level was prescribed for MEMRI studies. ECG-gated, fast low angle shot (FLASH) images were acquired before, during, and after Mn^{2+} infusion. Imaging parameters were: TE, 1.9 msec; TR, R-R interval (~120 ms); trigger delay, 1 ms; flip angle, 30° ; number of averages, 6; FOV $2.5 \times 2.5 \text{ cm}^2$; matrix size, 128×64 . Eight baseline images were acquired prior to Mn^{2+} injection. During the 30-min Mn^{2+} infusion and 30-min post-contrast periods, T_1 -weighted images were acquired at 1 min temporal resolution to track the kinetics of Mn^{2+} -induced contrast enhancement.

To assess the impact of Mn^{2+} on ventricular function, regular cine images were acquired at a temporal resolution of 9 frames per cardiac cycle before and after Mn^{2+} injection. Imaging parameters were the same as described above except with a larger data matrix of 128×128 and a smaller flip angle of 25° . Ejection fraction (EF) was calculated by tracing myocardial contours in the cine images using an in-house developed software (53, 54).

2.2.4 Image Processing

The MR images were analyzed using a Matlab-based software developed in our lab. All images were first zero-filled to 128×128 to achieve a nominal resolution of $195 \times 195 \mu\text{m}^2$. The left ventricular (LV) myocardium was segmented and considered as the region of interest (ROI). The average signal intensity (SI) in the ROI was normalized to that of the $MnCl_2$ phantom. Because of the slow Mn^{2+} delivery associated with intraperitoneal injection, only the last 20 min of Mn^{2+} injection period was linearly fitted to indicate the signal

enhancement rate. Linear regression fit was also continuously performed for every three adjacent time points to track the dynamics of signal enhancement rate during the entire 30 min Mn^{2+} injection period. Peak signal intensity was calculated as the average of the last ten images during the post-contrast period since intracellular retention of Mn^{2+} lasts for hours (4).

2.2.5 Statistical Analysis

All results were expressed as mean \pm standard deviation (SD). Unpaired student's *t*-test was used for intergroup comparison. A 2-tailed value of $P < 0.05$ was considered statistically significant.

2.3 Results

2.3.1 Animal Characteristics and Cardiac Function

The *adbn*^{-/-} mice and their WT littermates have similar body weights (BW) (28.5 ± 2.7 g and 29.0 ± 2.1 g, $p = \text{N.S.}$) and therefore were subject to similar Mn^{2+} doses of 13.3 ± 1.3 nmol/min/g BW and 13.5 ± 1.0 nmol/min/g BW, respectively.

The Mn^{2+} infusion did not lead to any significant changes in cardiac function (Fig. 2.1). Heart rate remains stable during the entire Mn^{2+} protocol (Fig. 2.1a). Specifically, for the *adbn*^{-/-} mice, the heart rate before Mn^{2+} and after infusion was 536 ± 33 bpm and 520 ± 32 bpm, respectively ($p = \text{N.S.}$). For the control mice, the heart rate was 551 ± 29 bpm and 518 ± 26 bpm before and after Mn^{2+} infusion, respectively ($p = \text{N.S.}$). Ejection fraction (EF) was also similar in both control and *adbn*^{-/-} mice before ($65.7 \pm 5.0\%$ and $68.6 \pm 3.2\%$) and after ($63.9 \pm 4.2\%$ and $68.4 \pm 2.8\%$) Mn^{2+} injection (Fig. 2.1b). In addition, there was no significant

difference in heart rate and EF between the control and $adbn^{-/-}$ mice both before and after Mn^{2+} injection.

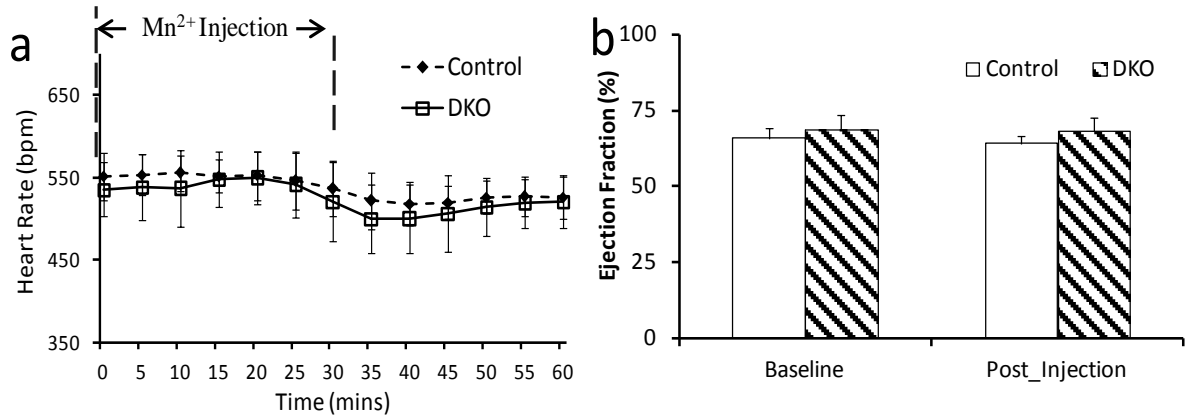


Figure 2.1 (a) Heart rate of the control and $adbn^{-/-}$ mice during the 30-min Mn^{2+} infusion and 30-min post-injection period; (b) Ejection fraction at baseline and at the end of post-contrast period. (Error bars = 1 SD.)

2.3.2 Dynamics of Contrast Enhancement

Representative T_1 -weighted images of a WT mouse heart are shown in Fig. 2.2a. The contrast enhancement was clearly visible at ~12 min of Mn^{2+} injection. The time courses of phantom-normalized signal intensities are shown in Fig. 2.2b. The signal enhancement in the $adbn^{-/-}$ mice was significantly faster than that of the controls most of the time during the Mn^{2+} injection (Fig. 2.2c). As a result, the averaged signal enhancement rate (43.8 ± 13.7 and 23.0 ± 12.3 %/0.5hr) and peak signal enhancement (37.3 ± 4.9 and 26.8 ± 4.0 %) was significantly greater in the $adbn^{-/-}$ mice ($P < 0.01$) (Fig. 2.2c). For both groups, the peak signal remained at the enhanced level during the post-contrast period, which is consistent with the previously reported long intracellular Mn^{2+} retention time (4, 7).

2.4 Discussion

The current study demonstrated the sensitivity of MEMRI to the alterations in calcium influx at baseline workload in a transgenic mouse model. Compared with their WT littermates, the 42% greater signal enhancement in *adbn*^(-/-) mice suggests an increased Mn^{2+} and Ca^{2+} uptake, which was in good agreement with the increased transsarcolemmal calcium current (I_{ca}) integral in our previous patch clamp measurement (52). Quantitatively, the 19 % increase in I_{ca} integral corresponded to a 90.4% faster signal enhancement rate observed in the *in vivo* MEMRI experiments (Fig. 2.2c). In addition, the plateau of signal enhancement during post-injection period was also consistent with the previous reports (4, 6, 31), suggesting the validity of the current measurements.

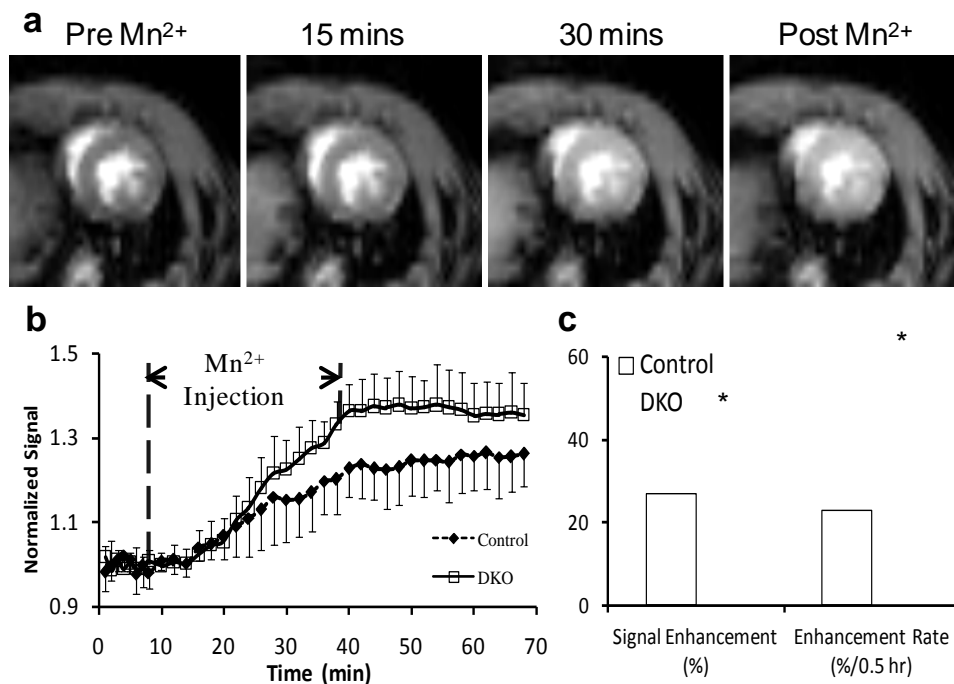


Figure 2.2 (a) Representative T_1 -weighted short-axis images acquired during Mn^{2+} protocol; (b) Time course of signal enhancement of the control and *adbn*^(-/-) mice; (c) The percentage and overall rate of signal enhancement. * $P < 0.05$ compared to age-matched controls.

The concern about the cardiac toxicity has been addressed in the current study as a preserved cardiac function was observed (Fig. 2.1). Similar with previous studies that have used comparable Mn^{2+} doses (6, 8, 26, 31, 35), this result provides direct evidence and support for future applications of MEMRI to *in vivo* studies. Furthermore, an even smaller Mn^{2+} dose may be used in clinical studies according to a previous study(55). With similar extracellular Ca^{2+} concentration and intracellular Ca^{2+} transient level, Ca^{2+} influx rate is approximately three times larger in human than rodents (56). Therefore, same level of Mn^{2+} may be accumulated for MRI detection with a three times smaller concentration of free Mn^{2+} in the extracellular space. The toxicity of Mn^{2+} may also be reduced at a cost of relaxivity by using its chelate form (MnDPDP) (57). Recent MEMRI studies in human have shown that the administration of 5 $\mu\text{mol/kg}$ BW MnDPDP did not cause any subjective symptoms or adverse effect (8, 58).

There are several experimental designs that deserve comment. First, the dead volume of the injection catheter in the current study is approximately $\sim 15 \mu\text{L}$ (6). Considering an injection rate of 200 $\mu\text{L/hr}$, the Mn^{2+} solution may travel in the catheter for the first 5 min of injection. This time should be excluded to better correlate the signal dynamics with physiological process. However, an accurate estimation of the time is extremely difficult since blood may also fill in part of the catheter. In addition, the injection site and blood circulation speed may also slightly vary for different animal studies, which complicates a quantitative correlation of the Mn^{2+} dynamics to Ca^{2+} influx rate. Therefore, an intravenous injection and a catheter with less dead volume may be used in future studies to reduce the variations in the early phase of injection. Nevertheless, over a long continuous injection

period, the later phase of the Mn^{2+} dynamics should faithfully represent the activity of L-type Ca^{2+} channels (6).

Another experimental design that is worth discussing is the data acquisition approach. In the current study, T_1 -weighted imaging was employed to estimate Mn^{2+} accumulation. However, T_1 -weighted signal intensity is nonlinearly related to Mn^{2+} concentration. Thus, the conversion process suffers from error propagation. Moreover, this nonlinear relationship may be biased by errors associated with B_0 field and T_2 inhomogeneities, which are extremely hard to predict. Therefore, such approach is suboptimal for the estimation of $\text{Mn}^{2+}/\text{Ca}^{2+}$ uptake dynamics. However, it can still provide valuable qualitative information about the Ca^{2+} channel activities in MEMRI studies. In the future, a direct measurement of R_1 may be used to overcome such limitation.

The last factor that may affect the accuracy of the current analysis is the lack of a kinetic modeling analysis. In each image voxel, the Mn^{2+} -induced changes in extracellular space and capillaries were counted towards the estimation of intracellular Mn^{2+} accumulation. A two-compartment kinetic model may be used to extract the transfer rate constants between all cellular compartments (8). However, the semi-quantitative or quantitative modeling analysis presents a high requirement on the accuracy of the data. Up to date, a robust MEMRI kinetic modeling analysis remains lacking.

Nevertheless, the consistence between the changes in Mn^{2+} -induced signal intensity and the L-type Ca^{2+} influx suggests that MEMRI may provide a powerful *in vivo* probe to sensitize the subtle alterations in L-type Ca^{2+} channel activity at baseline workload.

Chapter 3 A Fast T_1 Mapping Method for Dynamic Quantification of Mn^{2+}

Accumulation in Blood and Myocardium

3.1 Evaluation of Relaxivity under Different Physiological Conditions

3.1.1 Introduction

Estimation of the contrast agent distribution is often achieved by measuring T_1 or T_1 -weighted signal intensities in DCE-MRI. In most DCE-MRI studies, the linear coefficient that relates R_1 ($1/T_1$) and contrast agent concentration, also known as relaxivity (r_1), is assumed to be constant for the region of interest (ROI) during the entire DCE-MRI experiment (38). However, such assumption may not stand when there is a change in physiological environments, i.e., protein concentrations (11). Therefore, for quantitative DCE-MRI studies, it is imperative to evaluate the relaxivity values under a wide range of physiological conditions.

The ability of the paramagnetic contrast agent to reduce T_1 values mainly stems from the large local electromagnetic field generated by the unpaired electrons. When the electromagnetic field varies at the Larmor frequency of protons, the excited protons will effectively release the energy to the surrounding environments (lattice) in a 'resonant' state. In other words, the spin of the protons will relax back to its lowest energy state in a reduced time (T_1). The effectiveness of such process is dependent on a number of factors such as magnetic field strength, physiological environment, and the characteristics of the contrast agent itself (11). For instance, the chelated form of Mn^{2+} will have a lower relaxivity because Mn^{2+} ion is shielded from the surrounding water protons. The existence of Ca^{2+} may compete with Mn^{2+} for interaction with the surrounding molecules and therefore change the

relaxivity. A thorough evaluation of the relaxivity under different conditions can be tremendously time and resource consuming.

Nevertheless, most factors that affect relaxivity stay constant during the contrast agent administration period. In the current MEMRI studies, the most likely changing conditions are the protein concentrations associated with cell death and/or structural degenerations and the concentrations of Ca^{2+} since it may compete with Mn^{2+} for binding sites on proteins. Therefore, the relaxivity of MnCl_2 solution was evaluated over a wide range of protein and Ca^{2+} concentrations in the current study.

3.1.2 Methods

MnCl_2 solutions were freshly prepared on the day of imaging with concentrations ranging from 30 to 1000 μM . To evaluate the relaxivity at different protein concentrations, bovine serum albumin (Equitech-Bio Inc., Kerrville, TX) was used since it is the most abundant blood plasma protein. Since the normal *in vivo* albumin concentration ranges from 3 to 5.5 g/dL, a wider range of concentrations (1, 2.5, 5, and 10 g/dL) were used. To evaluate the effect of Ca^{2+} concentrations, relaxivity was measured in 2.5% albumin solutions with different Ca^{2+} concentrations (0 mM, 1.5 mM, and 10 times of Mn^{2+} concentrations). Each final solution was sealed in a 2.5 mL centrifuge tube. T_1 measurement was performed on a 9.4T vertical Bruker MR scanner (Bruker Biospin, Billerica, MA) at room temperature ($\sim 20^\circ\text{C}$) using the saturation recovery Look-Locker (SRL) method (59). Imaging parameters were as follows: TE, 1.9 ms; TR, 4.5 s; flip angle, 10° ; number of averages, 1; number of FLASH acquisitions, 25; acquisition intervals (τ), 180 ms; slice thickness, 1 mm; field of view (FOV), $2 \times 2 \text{ cm}^2$; matrix size, 128×128 . The estimated R_1 values and Mn^{2+} concentrations were linearly fitted. The slope was calculated as the relaxivity.

3.1.3 Results

Fig. 3.1 shows that relaxivity stayed at a relative constant level for different simulated physiological conditions. At high albumin concentrations (>2.5%), r_1 was slightly higher. However, the increasing trend was not monotonic. The fluctuation was only 4.1% when albumin concentrations fell within the normal physiological range (2.5% to 5%). The variations in Ca^{2+} concentrations did not cause a significant change in relaxivity either. For Ca^{2+} concentration ranged from 0 to the most common physiological value (1.5 mM), r_1 only changed by 2.9%. These results suggested that a constant relaxivity can be assumed to convert Mn^{2+} concentrations from T_1 values in the current MEMRI studies.

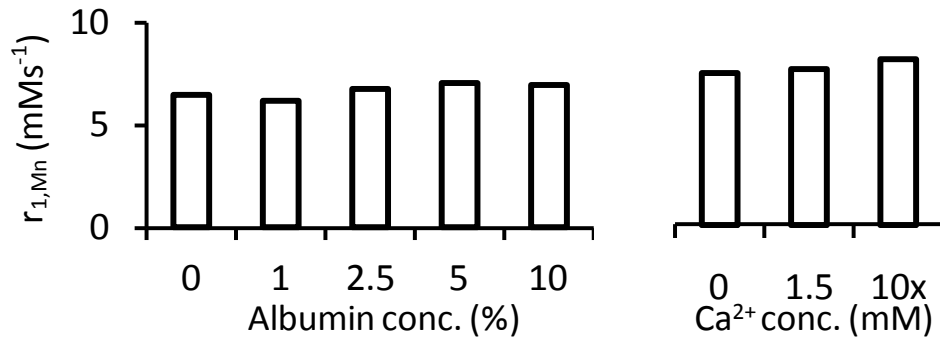


Figure 3.1 Relaxivity of MnCl_2 at different albumin and Ca^{2+} concentrations.

3.2 SRLI for Fast T_1 Mapping of Myocardium

3.2.1 Introduction

DCE-MRI plays an increasingly important role in cardiac imaging. The dynamics of contrast agent uptake and distribution have shown high sensitivity and specificity to many pathological changes that are not detectable by anatomical imaging (60, 61). Gd and Mn^{2+} are the two most popular T_1 shortening contrast agents that have been used in DCE-MRI

studies for the evaluation of myocardial viability and perfusion (62, 63). Typically, T_1 -weighted spin-echo or gradient-echo images are acquired at high spatial and temporal resolution to track the dynamics of signal enhancement induced by contrast agent accumulation. However, the existence of B_1 inhomogeneity hinders the direct quantification of contrast agent concentration from the T_1 -weighted images (64).

Previous research has shown a linear relationship between relaxation rate (R_1) and contrast agent concentration in a relatively wide range (31, 65). Hence, quantification of contrast agent concentration can be achieved by measuring T_1 changes directly (66, 67). However, the typical long data acquisition time for T_1 mapping has limited its practical use in DCE-MRI studies that require high temporal resolution (68). Therefore, the development of a rapid T_1 mapping method that enables quantification of the contrast agent distribution will greatly benefit the application of DCE-MRI.

Several fast T_1 mapping methods have been proposed. A commonly used method acquires gradient-echo images with variable flip angles to fit for T_1 (69, 70). Another similar approach uses the ratio image of a proton density-weighted image and a T_1 -weighted image to obtain the T_1 map (71). However, these techniques are susceptible to errors associated with an imperfect B_1 field (72). Although substantial effort has been devoted to correct for these errors (71, 73), these methods have found limited applications in the heart due to the cardiac motion and susceptibility difference between myocardium and blood. Alternatively, inversion recovery (IR), saturation recovery (SR), and Look-Locker methods track the dynamic recovery of longitudinal magnetization (M_z) for T_1 mapping and are inherently more tolerant to B_1 inhomogeneity. By sampling multiple time points along the recovery curve in each phase encoding step, the Look-Locker method is the most time efficient

method for T_1 mapping (74). With the aid of echo-planar (EPI)/segmented k-space imaging and/or parallel acquisition, T_1 mapping can be achieved within 30 s (68, 75-77). Recent studies using a modified IR Look-Locker method with EPI scheme was able to acquire T_1 maps of human hearts at a high spatial resolution (2x2 mm) within one breathhold (78, 79). However, the fast heart rate in small animals renders the implementation of EPI problematic. As a result, dynamic T_1 acquisition in small animal hearts remains a challenge (80).

In this study, we present a saturation recovery Look-Locker (SRLL) method that allows rapid T_1 mapping of mouse myocardium within 3 minutes. In contrast to the long repetition time required by the IRLM method, a shorter repetition time (TR) was used in SRLL to reduce imaging time. Simulation studies were employed for error analysis and parameter optimization. Validation was performed on both phantom and mouse hearts in vivo. The utility of SRLL was demonstrated in an in vivo manganese-enhanced MRI (MEMRI) study using a mouse model. Our results suggest that SRLL can provide fast, accurate cardiac T_1 mapping for DCE-MRI studies in small animals.

3.2.2 Methods

Imaging method and T_1 mapping

A schematic diagram of the SRLL pulse sequence is shown in Fig. 3.2. An ECG-triggered saturation module that consisted of three non-slice-selective 90° RF pulses was applied at the beginning of each phase encoding step, followed by ECG-triggered acquisition of k-space lines of N ($N=9\sim 11$) images using FLASH. This acquisition scheme yielded a TR of ~ 2.4 s for each phase-encoding step, which rendered a $\sim 85\%$ recovery of the longitudinal magnetization for a typical myocardium T_1 value (~ 1.2 s) before contrast agent injection.

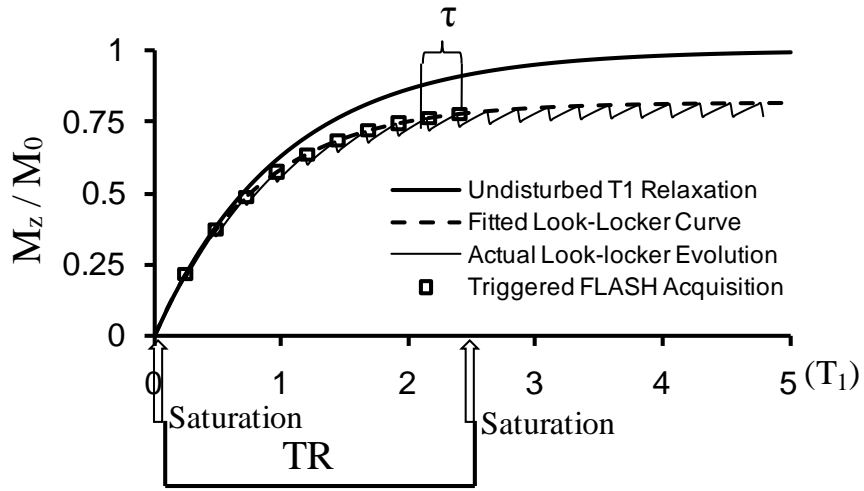


Figure 3.2 SRLL pulse sequence. An ECG-triggered saturation module is followed by N successive ECG-triggered FLASH acquisitions.

The signal evolution in Look-Locker acquisition has been derived in previous studies (81, 82). The recovery of the longitudinal magnetization before each excitation pulse can be described by an exponential function,

$$M(n) = M^* - (M^* - M(0)) \exp\left(-\frac{n\tau}{T_1^*}\right), \quad n = 1, 2, 3 \dots N \quad [1]$$

where $M(0)$ is the initial longitudinal magnetization immediately after the saturation pulses and is approximately zero. T_1^* is the effective longitudinal relaxation time constant and is related to T_1 , flip angle α and the interval τ by

$$\frac{1}{T_1^*} = \frac{1}{T_1} - \frac{\ln(\cos \alpha)}{\tau} \quad [2]$$

M^* is the effective equilibrium longitudinal magnetization and is related to the equilibrium longitudinal magnetization M_0 by

$$M^* = M_0 \frac{1 - \exp(-\tau / T_1)}{1 - \exp(-\tau / T_1^*)} \quad [3]$$

The first-order Taylor expansion of $\exp(-\tau / T_1)$ and $\exp(-\tau / T_1^*)$ leads to the following relationship between T_1 , T_1^* , M^* and M_0 (83).

$$T_1 = \frac{M_0}{M^*} \times T_1^* \quad [4]$$

In the current study, M_0 was obtained by acquiring a gradient-echo image with a TR at least 5 times of T_1 . Since M_0 is an intrinsic tissue characteristic that does not vary with contrast agent accumulation, a single measurement at baseline is sufficient for the entire DCE-MRI study. From Eq. 1, T_1^* , M^* , and $M(0)$ can be obtained by a three-parameter fitting to the measured signal $M(n)$. Consequently, Eq. 4 allows the determination of T_1 .

Error analysis and parameter optimization

While a short TR is desirable for fast T_1 mapping, insufficient coverage of the recovery curve leads to increased fitting errors (76). To evaluate the impact of reduced TR on T_1 estimation, simulation studies were performed on three different TR values (1.2, 2.4 and 6 s). A set of recovery curves with T_1 ranging from 0.2 s to 1.7 s was generated according to Eqs. 1-3, with a flip angle of θ_0 and a τ of 120 ms (comparable to the R-R interval in a mouse heart). A 5% random noise, similar to the signal-to-noise ratio (SNR) in vivo, was added to the data. T_1^* and M^* were determined by fitting Eq. 1 to the partial recovery data within 1.2 s, 2.4 s and 6 s. This process was performed 25 times for each curve. Consequently, T_1 was determined from Eq. 4. The differences between the theoretical T_1 values and the estimated T_1 values were analyzed using Bland-Altman method.

Further simulation studies were performed to evaluate the effects of the duration of τ on T_1 estimation. For a fixed TR value of 2.4 s, another data set was generated with $\tau = 240$ ms (comparable to 2 R-R intervals in a mouse heart) and used to derive T_1 as described above. The results were analyzed and compared to the above estimation with $\tau = 120$ ms.

The effects of heart rate fluctuation on the accuracy of T_1 estimation were also evaluated. Simulated recovery curves that reflected varied data sampling intervals were generated. Specifically, the signal intensity at the n^{th} data point was calculated using a time value that deviated randomly from the theoretical value of $n\tau$ by 5%, 10%, and 15%, respectively. A 5% random noise was also added to the simulated data. Curve fitting and comparison analysis were conducted as described above.

To further evaluate the accuracy of T_1 estimation at the presence of beat-to-beat variation, a simulation model was developed using a donut-shaped digital phantom. The phantom has four segments with T_1 values of 1, 1.2, 1.4, and 1.2 s, respectively (Fig. 3.4a). A random rotation of 0.2° was applied to the phantom image to simulate the variation in twist motion of the heart. Variation in myocardial displacement was simulated by applying a random 25 μm translation. To generate the saturation recovery images, each k-space line was simulated sequentially with rotation or displacement applied randomly to the digital phantom. The composite k-space images were Fourier transformed, and pixel-by-pixel curve fitting was performed to determine the T_1 values. The theoretical T_1 maps were subtracted from the estimated T_1 maps to evaluate the estimation errors.

Phantom studies

A multi-compartment phantom that consisted of distilled water dissolved with MnCl_2 at various concentrations ranging from 30 to 1000 μM was used for validation studies (Fig.

3.5a). The MR imaging experiments were performed on a horizontal 9.4T Bruker Biospec scanner (Bruker Biospin Co. Billerica, MA) equipped with a 35-mm birdcage coil. To evaluate the effect of flip angle on T_1 estimation, SRTL experiments were performed with a series of flip angles ranging from 6° to 18° . Other imaging parameters were: TR, 2.5 s; TE, 1.9 ms; number of averages, 1; number of FLASH acquisitions, 10; τ , 245 ms; slice thickness, 1 mm; field of view (FOV), $3 \times 3 \text{ cm}^2$; matrix size, 128×64 . Images were zero-filled to 128×128 during reconstruction. M_0 was measured with a long TR of 10 s. Standard spin-echo saturation recovery (SR) experiments were also performed for data comparison and validation (84). Various TR values (50, 90, 140, 200, 500, 800, 1100, 1700, 2400, 3350, 5000, 12500 ms) were used to sample the data on the entire longitudinal recovery curve. Image acquisition time was 3 min and 85 min for SRTL and SR methods, respectively.

In vivo studies

Four-month-old C57BL/6 mice ($n=6$) were used to validate the current method for in vivo manganese-enhanced MRI (MEMRI) studies. The animals were prepared as described previously (54). Briefly, animals were anesthetized with 1% isoflurane and placed in prone position. Heart rate was maintained at ~ 500 bpm with 0.8–1.8% isoflurane. Hot air was blown to the mouse with a blow dryer to keep body temperature at around 37°C , respiration, and body temperature were monitored and recorded by a physiological monitoring system (SA Instruments, Billerica, MA). MR images were acquired using the same coil as the phantom studies. The Mn^{2+} infusion protocol consisted of a 30-min intraperitoneal infusion of 126 mM MnCl_2 solution at a rate of 0.2 ml/hr, followed by a 15-min wash-out period. The animal protocol was approved by the Institutional Animal Care and Use Committee of the Case Western Reserve University.

The myocardium T_1 changes during the Mn^{2+} infusion protocol were tracked by ECG-triggered SRTL method with the following imaging parameters: TE, 1.9 ms; flip angle, 10° ; slice thickness, 1 mm; number of averages, 1; FOV, $2.5 \times 2.5 \text{ cm}^2$; matrix size, 128×64 . Images were zero-filled to 128×128 during reconstruction. The FLASH acquisitions were triggered every two heart beat, equivalent to a τ ranging from 200 to 270 ms. Based on the heart rate during each experiment, 9 to 11 images were acquired, leading to a TR of $\sim 2.5 \text{ s}$. For data validation, inversion recovery Look-Locker (IRLL) method was also applied before Mn^{2+} infusion and at the end of wash-out period (85). A 1 ms hyperbolic sech-shaped adiabatic pulse was employed to provide the 180° inversion. For each phase encoding step, 35 data points (TR $\approx 8 \text{ s}$) were acquired to cover the entire longitudinal recovery curve. Other imaging parameters were the same as those for SRTL scans. Total imaging time was 3 and 9 minutes for SRTL and IRLL, respectively.

Statistic analysis

All results were expressed as mean \pm SD. Paired student's t -test and Bland-Altman (86) analysis were performed to compare T_1 values measured by SRTL to those measured by standard SR method for in vitro studies or IRLL for in vivo studies, respectively. $P < 0.05$ was considered statistical significant.

3.2.3 Results

Simulation and error analysis

Figure 3.3 shows the effects of incomplete coverage of the recovery curve on the accuracy of T_1 estimation. For all 3 choices of TR, the estimated T_1 values exhibited a strong agreement with the theoretical value. Linear regression analysis showed a slope of 0.95, 0.99

and 1 for TR equals 1.2 s, 2.4 s and 6 s, respectively ($R^2 = 0.99$) (Fig. 3.3a-c). SD for all T_1 values was $<12\%$ with a moderate (2.4 s) or long (6 s) TR (Fig. 3.3f & 3.3g). However, due to limited coverage of the recovery curve with a short TR (1.2 s), estimated T_1 values showed large variations ($SD > 20\%$) for T_1 longer than 1.1 s (Fig. 3.3e). These results suggested that 2.4 s TR can provide sufficient coverage of the magnetization recovery for accurate estimation of T_1 changes in DCE-MRI experiments. Therefore, a TR of 2.4 s was used in all subsequent studies.

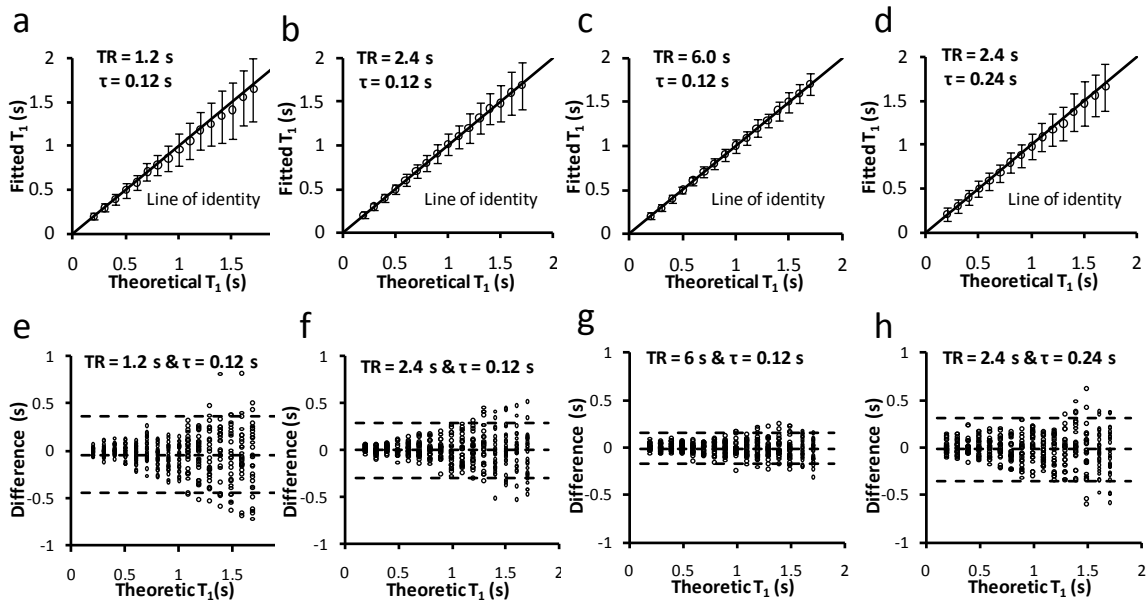


Figure 3.3 Simulation of the effect of TR on T_1 estimation. **a-d.** Fitted T_1 versus theoretical T_1 . The error bar is the standard deviation from 25 simulations. **e-h.** Bland-Altman plots of the difference between fitted T_1 and theoretical T_1 . The middle dotted line is the mean of the difference. The upper and bottom dotted lines are the mean plus and minus two times of the standard deviation, respectively.

The rapid switching of imaging gradients during data acquisition interfered with the ECG signal, rendering ECG triggering less reliable. Alternatively, triggering on every two heart beats enabled unambiguous detection of the QRS complex. However, it also led to doubled sampling interval and less data points for curve fitting. To evaluate the accuracy of

doubling sampling interval, T_1 was estimated using a TR of 2.4 s and a τ of 240 ms that is comparable to two R-R intervals in mice (Fig. 3.3d&h). Compared with the T_1 estimated with a τ of 120 ms (Fig. 3.3b&f), similar accuracy and SD were observed. Therefore, a two-beat triggering scheme was used in the in vivo studies to ensure consistent data sampling intervals.

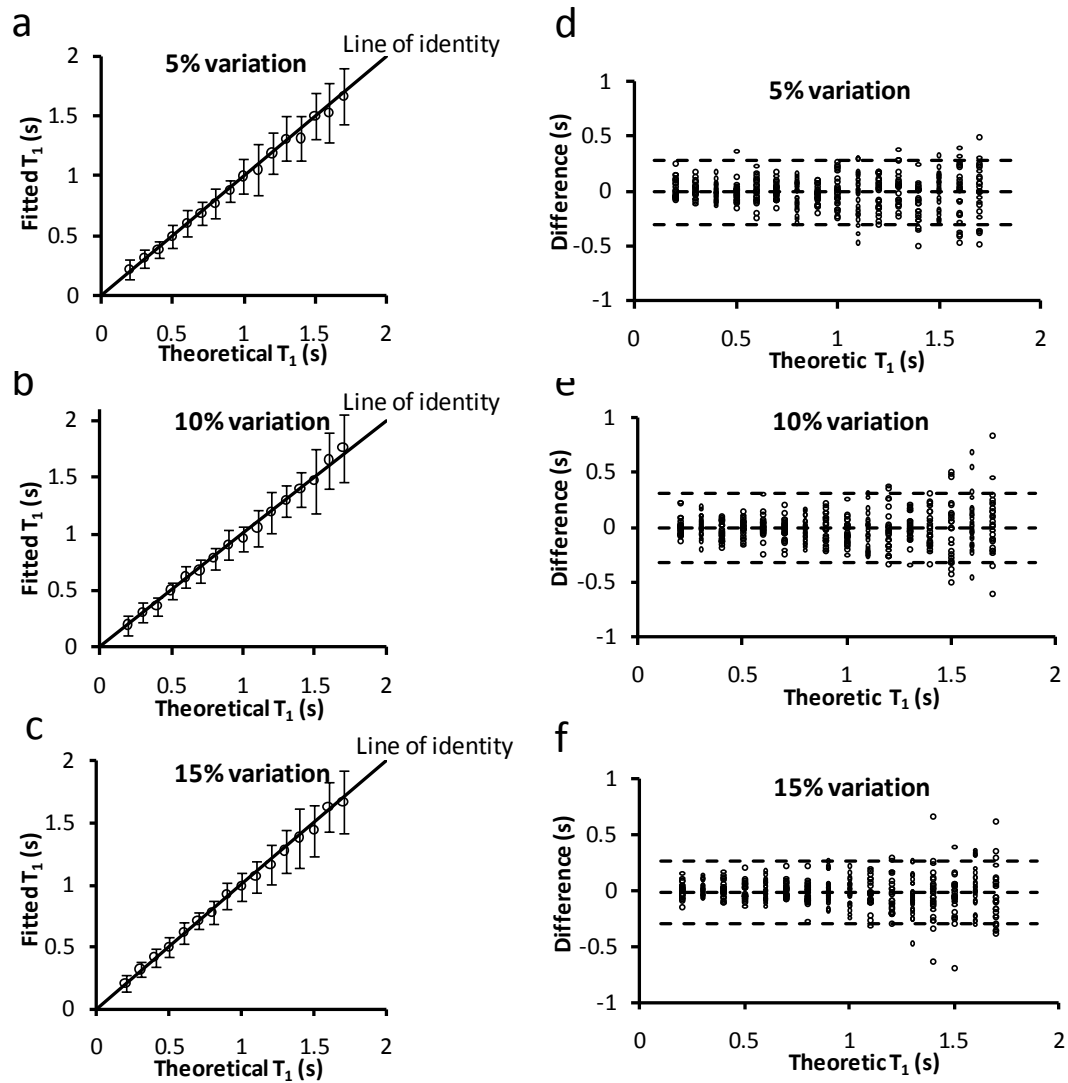


Figure 3.4 Simulation of the effect of τ fluctuation on T_1 estimation with TR = 2.4 s and $\tau = 0.24$ s. **a-c.** Fitted T_1 versus theoretical T_1 . The error bar is the standard deviation from 25 simulation runs. **d-f.** Bland-Altman plots of the difference between fitted T_1 and theoretical T_1 . The middle dotted line is the mean of the difference. The upper and bottom dotted lines are the mean plus and minus two times of the standard deviation, respectively.

The robustness of SRLM method to heart rate fluctuation is shown in Fig. 3.4. For heart rate variation of up to 15%, there was a strong agreement between the estimated and theoretical T_1 values (Fig. 3.4a-c). Bland-Altman analysis further showed a less than 5% ($P > 0.1$) deviation from the theoretic values for all three conditions (Fig. 3.4d-f). Since heart rate fluctuation is normally within 10% during the acquisition of a T_1 map (< 3 min), these data suggested that SRLM was capable of providing reliable T_1 estimation for most in vivo studies.

Estimation errors associated with beat-to-beat variations in translational and rotational motion are illustrated in Fig. 3.5. Displacement of up to $25 \mu\text{m}$ showed minimal effects on T_1 estimation (Fig. 3.5b&e). Errors due to random rotation (0.2°) were slightly larger ($\sim 5\%$), with the largest errors occurred at the border zone of 0.8 s and 1.2 s segments (Fig. 3.5c&f). With both rotational and translational motion present, estimation error further increased to 6% (Fig. 3.5d&g). Part of the estimation errors can also arise from a non-physiologic phantom with sharp changes in T_1 values.

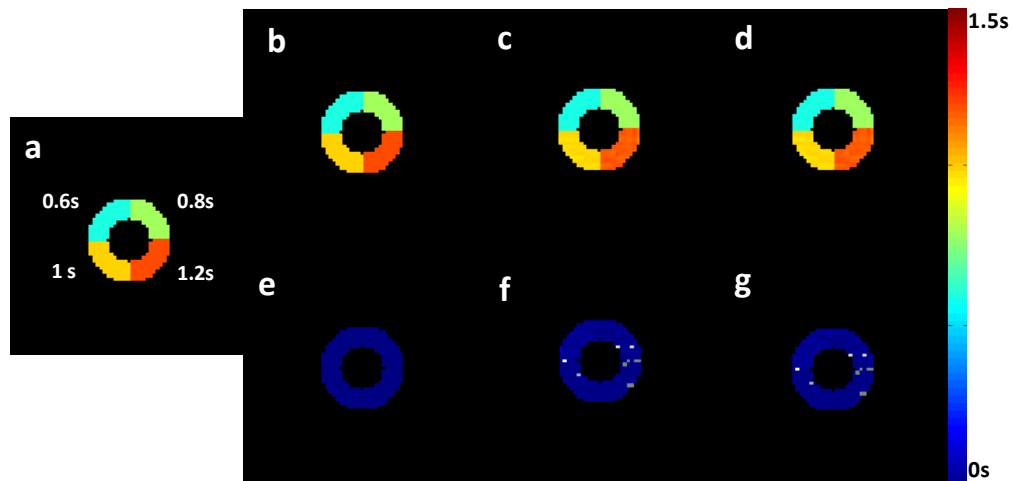


Figure 3.5 Simulation of the estimation errors caused by beat-to-beat variations in rotational and translational motion. **a.** Digital phantom with four segments of different, representative T_1 values. **b-d.** Estimated T_1 maps with random translational motion (b), rotational motion (c), and both rotational and translational motion (d) incorporated, respectively. **e-g.** Difference maps between theoretical and fitted T_1 maps (b-d), respectively.

Phantom study

The T_1 -weighted image and the T_1 map of the phantom are shown in Fig. 3.6. Regression analysis showed a linear relationship ($R^2 = 0.99$) between R_1 and Mn^{2+} concentration of up to 1000 μM , with a slope (relaxivity) of $6.4 (s\text{ mM})^{-1}$. To investigate the effect of flip angle on T_1 estimation, SRTL measurement was performed with flip angles ranging from 6° to 18° (Fig. 3.6d). For phantoms with 100 μM or higher Mn^{2+} concentration ($T_1 < 1.1s$), all flip angles yielded similar T_1 estimation compared with those measured by the standard SR method (Fig. 3.6d, horizontal dashed lines). SRTL estimated T_1 showed greater deviation from that measured by SR for 30 μM Mn^{2+} solution with a T_1 of 2 s. The largest deviation (9.6%) occurred when flip angle was 18° . While a larger flip angle provided better SNR, it also led to greater estimation error. A flip angle of 10° provided the best tradeoff between SNR and T_1^* contrast, leading to accurate T_1 estimation with small SD. Therefore, it was chosen for the in vivo experiments.

In vivo study

Fig. 3.7a-c shows representative FLASH images acquired at 2τ , 4τ , and 10τ after the saturation module. The progressive increase in myocardial signal intensity reflected the recovery of longitudinal magnetization and was used to derive the T_1 maps. A quantitative comparison of the T_1 maps showed no difference in T_1 estimation between SRTL and IRTL methods both before and after $MnCl_2$ injection (Fig. 3.7d-e).

Representative T_1 maps before and after Mn^{2+} infusion and the dynamics of R_1 changes are shown in Fig. 3.8. Compared with the T_1 maps at baseline (Fig. 3.8a), T_1 reduction over the whole LV area was observed at the end of 30-mins Mn^{2+} infusion (Fig.

3.8b). Correspondingly, R_1 increased from the baseline value of $0.84 \pm 0.07 \text{ s}^{-1}$ to $2.01 \pm 0.33 \text{ s}^{-1}$, with the half maximum R_1 reached at 23 min after Mn^{2+} infusion started (Fig. 3.8c).

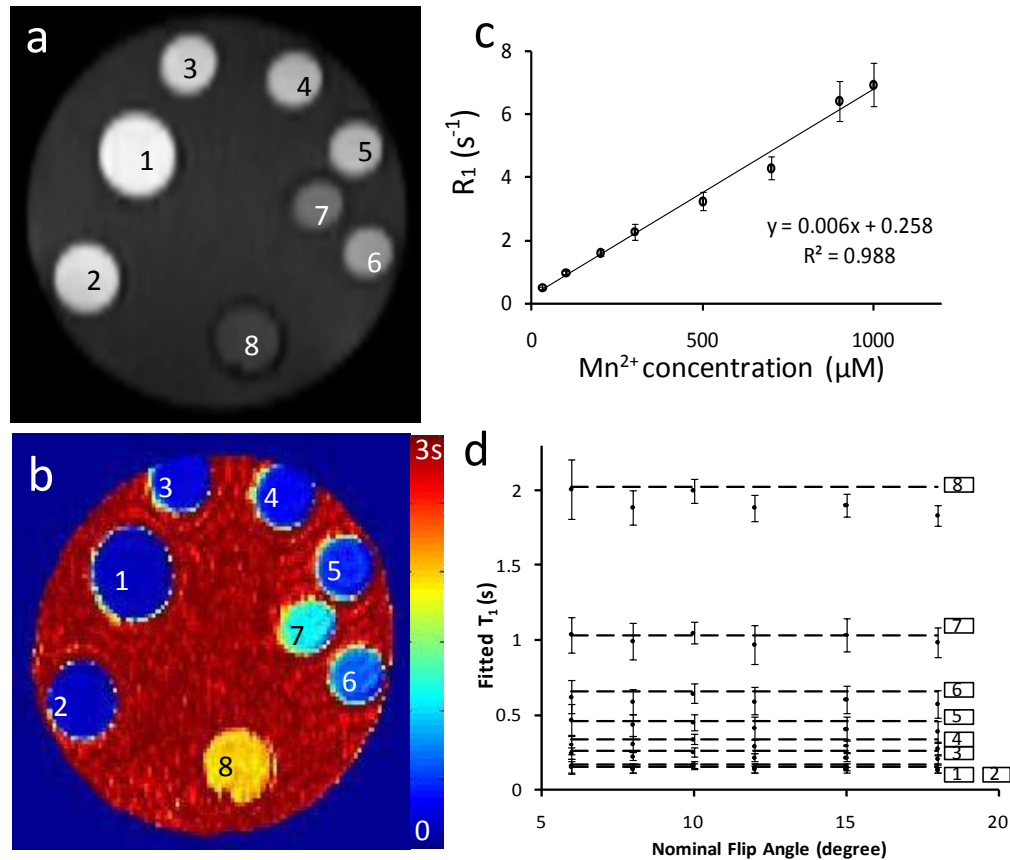


Figure 3.6 Phantom study. **a&b.** T_1 -weighted image and T_1 map of the phantom tubes, respectively. Phantoms 1 to 8 contained MnCl_2 solutions with the following concentrations (in mM): 1000, 900, 700, 500, 300, 200, 100, and 30. **c.** Longitudinal relaxation rate constant (R_1) versus Mn^{2+} concentration. **d.** T_1 values measured with different flip angles. The horizontal lines are the T_1 values measured by the standard SR method.

3.2.4 Discussion

Previously, inversion recovery Look-Locker method has been developed for fast T_1 mapping in vivo (68). Accurate T_1 mapping using inversion recovery can only be achieved with either complete recovery of the longitudinal magnetization via a long TR ($>5T_1$), or by

establishing a steady-state such that the longitudinal magnetization immediately before the inversion pulse is the same for each phase-encoding step. While acquisition with long TR suffers from low temporal resolution, the requirements of cardiac triggered acquisition and variations in heart rate prevent the establishment of a steady-state in a mouse heart. By using robust saturation pulses, our current method is equivalent to establishing an initial “steady-state” longitudinal magnetization of zero. This approach can effectively eliminate heart rate induced variations in initial magnetization. By sampling only the initial portion of the recovery curve, the SRLL method can greatly improve the temporal resolution for DCE-MRI studies.

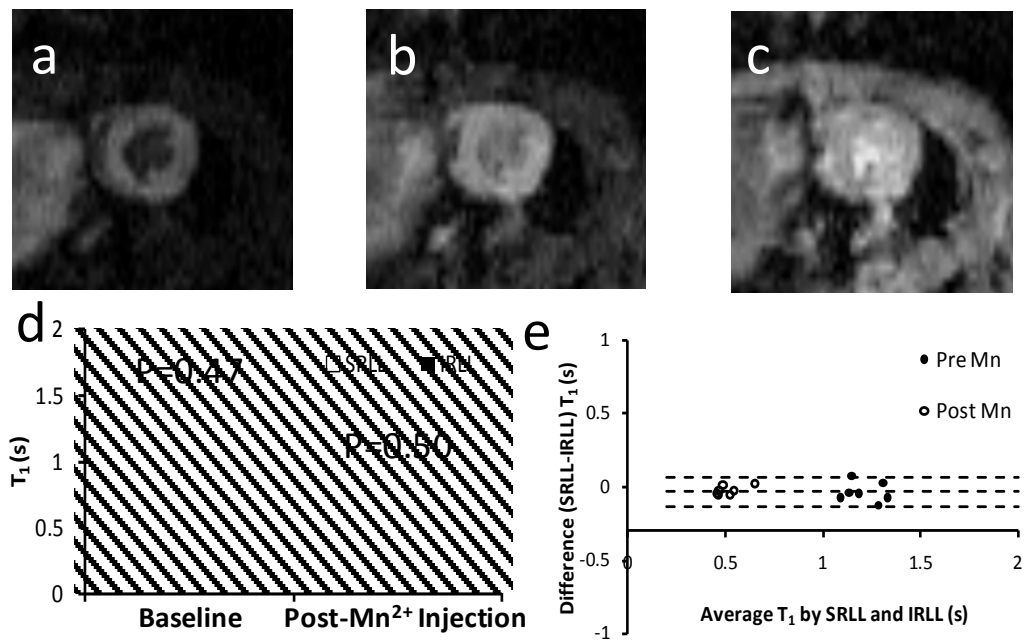


Figure 3.7 In vivo T₁ mapping. **a-c.** T₁-weighted images acquired at 2τ, 4τ, and 10τ after the saturation pulses, respectively. **d.** Mean T₁ values of the LV myocardium measured by SRLL and standard inversion recovery Look-Locker (IRLL) method before and after Mn²⁺ injection. **e.** Bland-Altman plot comparing T₁ values measured by SRLL method and IRL method.

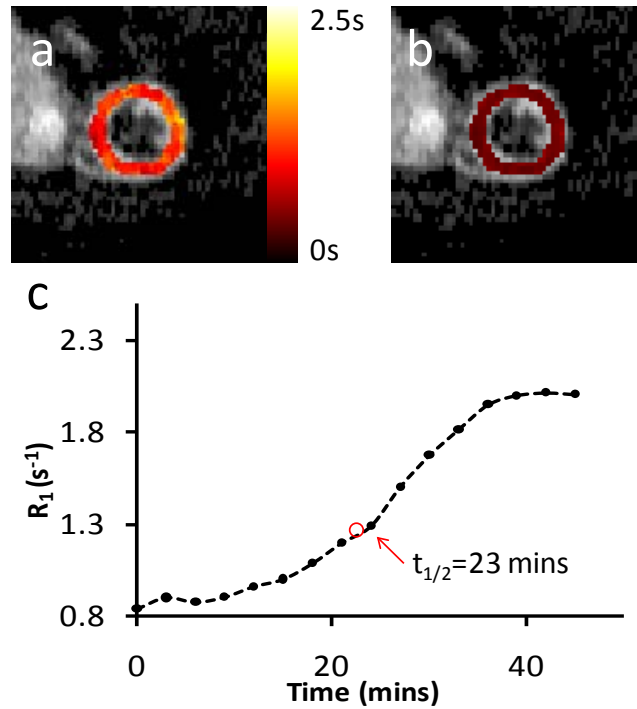


Figure 3.8 R_1 changes in dynamic MEMRI study. **a&b.** Representative T_1 maps of a heart pre- and post- $MnCl_2$ injection, respectively. **c.** Time course of R_1 changes tracked by SPLL at a temporal resolution of 3 min.

Both SNR and the dynamic range of the signal can affect the accuracy of T_1 estimation (84). While a shorter TR is desirable for higher temporal resolution, the dynamic range of the signal is reduced with shortened coverage of the recovery curve. Karlsson et al suggested that a TR of $>2T_1$ was needed for accurate T_1 estimation (82). Our error analysis showed similar findings. With a SNR (≈ 20) that was lower than the experimental in vivo SNR (~ 26), our simulation results suggested that a TR of 2.4 s was sufficient to yield accurate estimations for a wide range of T_1 values (0.2~1.7 s) that encompassed possible myocardium T_1 changes in DCE-MRI experiments for magnetic field strength up to 11.7 T (87). In the current study, image acquisition was triggered every two heart beats to avoid mis-triggering caused by the interference of switching gradients with the ECG signal. Such an acquisition scheme leads to reduced data points that can be acquired within the same

period of time if acquisitions were triggered at every heart beat. However, our simulation results suggest that both acquisition schemes should yield similar accuracy in T_1 estimation (Fig. 3.3b&d). Further, triggering every two heart beats has the additional benefit of less energy deposition.

In the current study, effective longitudinal relaxation time constant (T_1^*) and equilibrium magnetization (M^*) were determined by fitting Eq. [1] to MRI data. Theoretically, T_1^* is related to T_1 , the flip angle, and the sampling interval as shown in Eq. [2], which allows the calculation of T_1 from T_1^* . However, actual flip angle often deviates from its nominal value because of the B_1 inhomogeneity (73). Although various methods for B_1 mapping have been proposed (88, 89), their application to the fast beating mouse hearts are still problematic. Alternatively, T_1 can be calculated directly from T_1^* , M^* , and M_0 using Eq. [4], which is derived from the first-order Taylor expansion of $\exp(-\tau/T_1)$ and $\exp(-\tau/T_1^*)$. It should be noted that this approach introduced a 0.3~0.7% underestimation of the T_1 values with the current imaging parameters. This systematic underestimation was more pronounced with larger flip angles (Fig. 3.6d). Although a larger flip angle has the potential benefit of increased SNR, this underestimation can increase from 0.7% to 7% if a 30° flip angle is used instead of 10° . In addition, larger flip angles also reduce T_1^* -associated imaging contrast, leading to reduced dynamic range for curve fitting (90). Our phantom results showed that T_1 estimation was accurate for nominal flip angles ranging from 6° to 15° for a $T_1 < 2$ s. This estimation is comparable to that reported in previous studies (83, 91, 92).

The validity of the current method was demonstrated by a strong agreement with the measurement using standard magnetization recovery methods in both phantom and in vivo studies. The baseline myocardium T_1 value was also similar to that reported in the literature

(7, 93). The measured time course of R_1 changes exhibited a similar dynamics as compared to previous cardiac MEMRI studies employing T_1 -weighted methods (6, 26). According to the study by Waghorn and colleagues (31, 31, 65), the observed R_1 changes in our current study indicated that total Mn^{2+} uptake at the end of $MnCl_2$ infusion protocol was around 24 $\mu\text{g/g}$ dry wt. The constant R_1 level during the wash-out period was supported by previous findings that intracellular Mn^{2+} retention may last for hours (31, 65).

In summary, a fast cardiac T_1 mapping method using saturation recovery Look-Locker pulse sequence (SRLL) was developed and validated for studies employing small animal models. Each T_1 map can be acquired within 3 min without the aid of parallel imaging or segmentation/EPI techniques. The robustness and accuracy of this method were validated in both phantom and in vivo experiments. The successful demonstration in the MEMRI experiment shows the potential of the SRLL method for practical applications.

3.3 SRLL for Rapid Quantification of Arterial Input Function (AIF)

3.3.1 Introduction

DCE-MRI plays an important role in delineating pathophysiological conditions, i.e., angiogenesis (94) and myocardial infarction (62). To obtain accurate DCE-MRI analysis, the distributions of contrast agent in both blood and tissue need to be sampled at high temporal and spatial resolution. However, the measurement of the contrast agent in blood plasma (C_p), also referred to as arterial input function (AIF), is notoriously challenging (38).

Currently, there are four approaches to measured AIF. The direct blood withdrawal method is commonly used in human studies (95, 96). However, only few sampling points is allowed for mouse studies using such approach because of the limited blood pool size (~

2ml). The second approach uses the averaged AIF from a small cohort of subjects for all subsequent studies (97, 98). However, it suffers from errors caused by inter- and intra-subject variations. The third approach uses the contrast agent distribution at a reference region (e.g. muscle) to infer the AIF at the target tissue (99). However, errors may arise from the difference in blood perfusion at different sites of the body. The last approach estimates the contrast agent concentration directly from the non-invasive MRI dataset (100). Most studies along this line used T_1 -weighted signal intensity for the estimation (101). However, it is inevitably subject to errors associated with field and T_2 inhomogeneities.

Alternatively, a direct measurement of T_1 can provide objective quantification of the contrast agent content because of the direct relationship between them (65). However, the long imaging time has limited such approach in DCE-MRI studies (81). Fast T_1 mapping is challenging, especially for the imaging of mouse heart because of the extremely fast heart beat and blood circulation. Recently, Heilmann et al proposed a saturation recovery multi-gradient-echo turbo-FLASH method to simultaneously acquire T_1 values of the blood and myocardium (102). However, the two-point fitting of T_1 was still subject to field inhomogeneities. To achieve a robust T_1 estimation that is independent of hardware and operation variations, we developed an ECG-triggered saturation recovery Look-Locker method (59). However, according to previous simulations (59), a long imaging time may be required due to the long blood T_1 value ($\sim 1.7s$) (8, 103). In addition, the accuracy of the measurement may be degraded by the flow of unsaturated blood spins into the imaging slice (102).

In the current study, the previously reported SRLL method was modified to accommodate the above concerns for simultaneous measurement of both blood and

myocardial T_1 in mice. Specifically, the configuration of RF coils was changed to achieve whole body saturation with high SNR. The signal recovery model for the fitting of blood T_1 was also revised to accommodate the fast blood circulation. A two-dose manganese-enhanced MRI (MEMRI) study was performed on mice to validate the blood T_1 measurement based on the known linear relationship between Mn^{2+} concentration and changes in R_1 (ΔR_1). The chemical analysis method (AAS) was used to measure absolute Mn^{2+} concentrations (C_{Mn}). A consistent ratio in ΔR_1 and C_{Mn} between the two dose groups was considered as the evidence to demonstrate the accuracy of the blood T_1 measurement.

3.3.2 Methods

Modified SRLL method for T_1 mapping

The previously reported SRLL method samples the longitudinal magnetization (M_z) recovery curve by implementing a saturation module at the beginning of each phase-encoding step, followed by a series of ECG-triggered fast low-angle shot (FLASH) acquisitions (59). To extend it for blood T_1 measurement, the following two modifications were made in the current study. First, to eliminate the potential errors caused by the inflow of unsaturated blood spin, whole-body saturation was generated. A birdcage coil (Bruker, Billerica, MA) that was usually used for rat imaging (18 cm long and 6.9 cm in diameter) was employed as the transmitter. To improve the SNR, a circular surface coil with a diameter of 3 cm (Bruker, Billerica, MA) was taped tightly to the mouse chest as the receiver. Second, a conventional saturation recovery (SR) signal model was used for the fitting of blood T_1 . In Look-Locker acquisition, the signal recovery is disturbed by continuous samplings. Therefore, the signal evolution is dictated by the effective relaxation time

constant (T_1^*) and effective equilibrium magnetization (M^*). However, such disturbance does not apply to the blood in LV since blood is pumped out of the imaging slice after each ECG-triggered acquisition.

In vivo MEMRI experiment

4-month old C57BL/6 mice were used for validation. The mice were divided into two groups, which were subject to 30-min intravenous infusion of Mn^{2+} at rates of 7 (n = 6) and 14 nmol/min/g body weight (BW) (n = 8), respectively. Both groups were also subject to a 30-min wash-out period. Other animal handlings were similar as described before (59). The animal protocol was approved by the Institutional Animal Care and Use Committee of the Case Western Reserve University.

The imaging was performed on a 7T horizontal Bruker scanner (Bruker Biospin, Billerica, MA) with the RF coils configured as described above. T_1 maps of a short-axis slice at mid-ventricle were continuously acquired using SRTL during the Mn^{2+} infusion protocol. The imaging parameters were as follows: TE, 1.7 ms; TR, ~ 2.5 s; flip angle, 10°; slice thickness, 1.5 mm; number of averages, 1; FOV, 3x3 cm²; matrix size, 128x64. Images were zero-filled to 128x128 during reconstruction. The acquisition time of each T_1 map was 3 min. During data processing, the T_1 values of blood and myocardium were calculated by pixel-wise fitting of the signal intensities to the SR and SRTL signal models, respectively.

Measurement of absolute Mn^{2+} concentration

The absolute Mn^{2+} concentration was measured by the AAS method. Animals were divided into five groups. One group (n = 2) served as the reference group to provide baseline Mn^{2+} concentrations in blood and myocardium. Two groups were subject to 30 min infusion of Mn^{2+} at rates of 7 (n = 4) and 14 nmol/min/g body weight (BW) (n = 5), respectively.

Blood withdrawal and heart extraction was performed at the end of infusion to provide peak Mn^{2+} concentrations. The last two groups ($n = 4$) were used to provide Mn^{2+} concentrations at washout period. Therefore, same 30 min Mn^{2+} infusion protocol was administered, followed by a 30 min washout period. The blood and heart was sampled at the end of the washout period.

Following the excision, all blood and heart samples were placed in oven for 3 hours at 600°F. The blood and heart ashes were first dissolved in 100% nitric acid and then diluted to 20% for the measurement on an atomic absorption spectrophotometer (Buck Scientific, East Norwalk, CT).

3.3.3 Results

Demonstration of whole-body saturation

Fig.3.9 shows the saturation effect from the two different sized RF coils. The effective saturation region rendered by the coil that usually is used for mouse imaging (5.4 cm) was significantly shorter than that generated by the rat coil (9.4 cm) (Fig. 3.9b). Since a normal 4 month old mouse has a body length of 8 cm, robust whole body saturation can be achieved by using the rat coil. As a result, in the *in vivo* experiment, the error caused by the inflow of unsaturated blood spins was eliminated, rendering a consistent signal recovery curve (Fig. 3.9c).

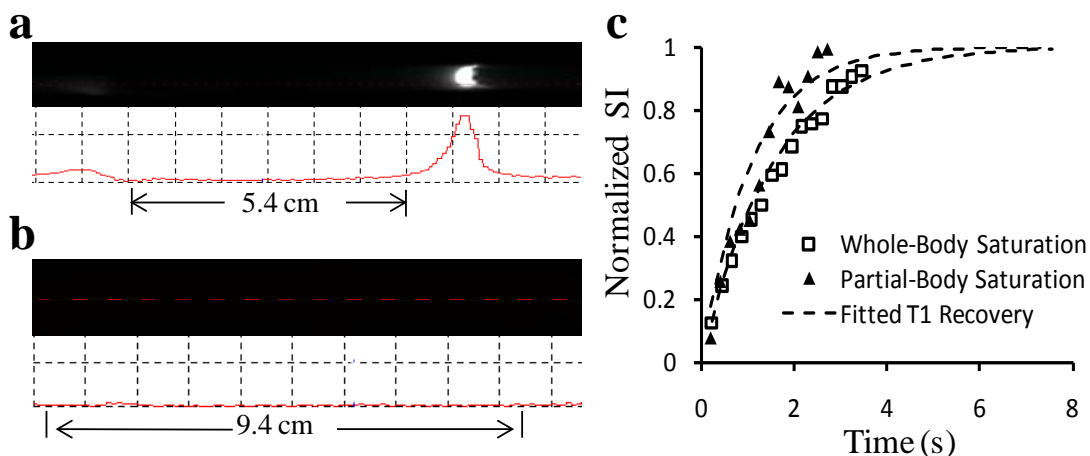


Figure 3.9 (a)&(b) Signal intensity profile along the long axis of the cylindrical water phantom. Partial-body and whole-body saturation was achieved by the mouse coil (a) and rat coil (b), respectively. (c) Normalized signal intensity (SI) evolution of the left ventricular blood after saturation preparation in mouse.

In vivo MEMRI

Figure 3.10 shows R_1 dynamics in the *in vivo* MEMRI experiment. The estimated R_1 values of blood ($0.57 \pm 0.06 \text{ s}^{-1}$) and myocardium ($0.75 \pm 0.11 \text{ s}^{-1}$) at baseline were consistent with those reported in literature (31). Mn^{2+} injection led to an increase in R_1 in both blood and myocardium (Fig. 3.10a). Compared with those in the low Mn^{2+} dose group, the increases of R_1 was 2.2 times greater for both blood ($0.38 \pm 0.20 \text{ s}^{-1}$ vs $0.84 \pm 0.28 \text{ s}^{-1}$) and myocardium ($0.60 \pm 0.30 \text{ s}^{-1}$ vs $1.36 \pm 0.33 \text{ s}^{-1}$) in the high Mn^{2+} dose group (Fig. 3.11a&b). While blood R_1 returned to baseline values at the end of washout period, myocardial R_1 remained high, reflecting the long intracellular Mn^{2+} retention time (Fig. 3.11a&b).

Absolute Mn^{2+} concentration

The absolute Mn^{2+} concentration measured by AAS was consistent with the above SRLM measurements. Compared with the low dose group, injection of Mn^{2+} solution at high dose raised the Mn^{2+} concentration in blood and myocardium by 2.4 and 2.1 times,

respectively (Fig. 3.11c&d). Both ratios were close to those of the R_1 changes (~ 2.2). At the end of the washout period, nearly all Mn^{2+} in the blood were cleared out, while the concentration in myocardium remained the same as the end of Mn^{2+} infusion (Fig. 3.11c&d). The good agreement in ΔR_1 and Mn^{2+} concentrations obtained from SRLL and AAS measurements confirmed the validity of the SRLL method for simultaneous quantification of AIF and myocardial T_1 .

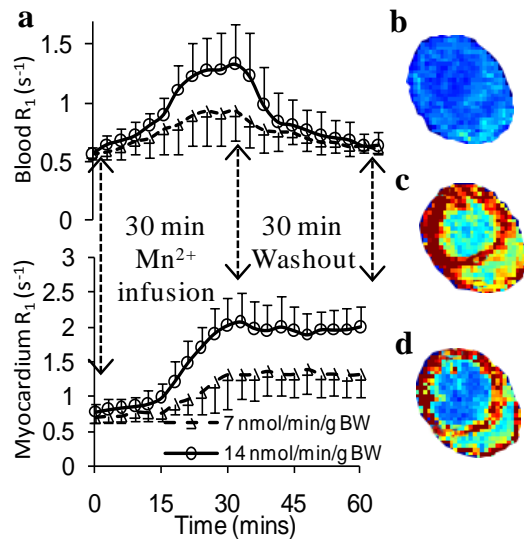


Figure 3.10 (a) Time courses of blood and myocardium R_1 in response to Mn^{2+} injection; (b) – (d) R_1 maps acquired at baseline (b), end of 30 min infusion (c) and end of 30 min washout period (d).

3.3.4 Discussion

In the current study, a fast and accurate measurement of blood T_1 was achieved by modifying the RF coil configuration and signal recovery model. Therefore, the current modified SRLL method can provide simultaneous measurement of myocardial T_1 and AIF for quantitative MEMRI analysis.

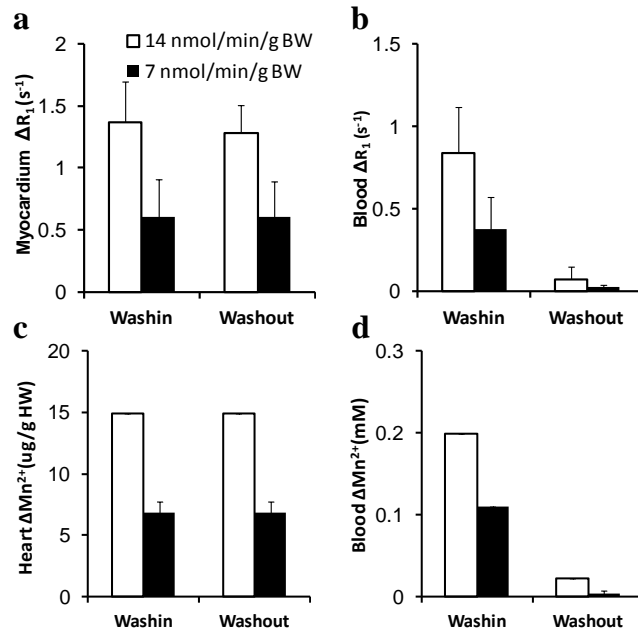


Figure 3.11 Changes in ΔR_1 and absolute Mn^{2+} concentration at the end of injection and washout sessions.

The use of an oversized volume coil for transmitting in the current study was urged by the need for whole body saturation to accommodate the fast blood circulation. In mouse, the circulation time is only ~ 9 s according to its cardiac output (13.3 ± 3.3 ml/min) (53) and blood volume (~ 2 ml) (38). Assuming a constant flow speed, the averaged blood flow rate is 1.7 cm/s for an average body length of 8 cm. Therefore, whole body saturation is needed to avoid unsaturated blood flowing into the imaging slice within the time frame of each acquisition cycle (~ 2.5 s). On the other hand, the enlarged coil size resulted in decreased SNR. Thus, a surface coil was used as receiver to improve the SNR from the suboptimal level of 15 to 22. This configuration of RF coils has been demonstrated to work well for small rodents (Fig. 3.9). For clinical studies, the traditional single coil configuration may suffice as the blood circulation is significantly slower (~ 60 s). However, a robust feasibility

evaluation cannot be achieved until the effective saturation region of the transmit coil is identified.

Ideally, the site of AIF measurement should be at the blood vessel that directly supplies the tissue of interest. In the current study, the most desired measurement site is the coronary artery because of its adjacency to the myocardium. However, localization of coronary artery can be extremely challenging because of the SNR and time constraints for high spatial resolution imaging. As the immediate upstream source of coronary artery blood, blood in LV cavity has similar Mn^{2+} concentration. At diastole, blood in LV cavity also had little turbulence. Therefore, determination of AIF from LV cavity blood is an optimal choice for the current application.

To the best knowledge of the authors, the indirect validation of blood T_1 measurement using two-dose MEMRI experiments was never performed before and therefore deserves further discussion. The prerequisite for such an approach is that relaxivity remains the same in all measurements. Another assumption is that the measurement of C_{Mn} is accurate. Once these two assumptions are validated, the accuracy of T_1 measurement can be demonstrated by comparing the ratios of C_{Mn} and ΔR_1 in the two doses groups. Based on the well recognized linear relationship between C_{Mn} and ΔR_1 , the ratio of accumulated C_{Mn} should be the same as the ratio of ΔR_1 in response to injection of two different doses of Mn^{2+} . In the current study, the first assumption about the stability of relaxivity was demonstrated in an earlier experiment (Fig. 3.1). The robustness of AAS measurement for Mn^{2+} concentration was also demonstrated in previous reports (104), which validated the second assumption. Therefore, the design of the current validation experimental is sound and rigorous.

Although not exactly the same, the ratio of SRTL measured ΔR_1 (~2.2) was fairly close to that of the AAS measured C_{Mn} to demonstrate the accuracy of the SRTL measurement (Fig. 3.11). The small discrepancy may be attributed to individual differences since the SRTL and AAS measurements were performed in separate cohorts of mice. It may also be caused by the difference in sampling time. For SRTL measurement, although central encoding scheme was adopted, T_1 estimation was inevitably affected by the variation in T_1 value over the entire sampling period (~ 3 min). For AAS study, the exact time of blood withdrawal was hard to predict due to the variations in manual operation. During the withdrawal process, Mn^{2+} circulation was also interfered and may consequently affected Mn^{2+} concentration in the blood.

Chapter 4 A Model-Based Compressed Sensing Method for Fast T_1 mapping

4.1 Introduction

The diagnostic power of MRI stems from the measurements of various parameters that are characteristic of the intrinsic tissue structure and physiology, e.g., the longitudinal (T_1) and transverse (T_2) relaxation time constants, the diffusion coefficients, and the kinetic parameters of contrast agent accumulation. Fast and direct measurements of these parameters can provide unique delineation of the physiological systems and thus are desirable in a wide range of applications (38, 105, 106). Multi-acquisition schemes are commonly used for robust parameter estimation. However, this often leads to a long scan time and becomes a major challenge for the application of MR parametric mapping.

Echo planar imaging (EPI) and parallel imaging are the two most widely used methods in fast MR imaging. In large mammals, fast T_1 and T_2 mapping can be achieved within a minute using these methods on clinical scanners (91, 107, 108). However, for small animal imaging at high field, implementation of EPI can be problematic because of the increased field inhomogeneity associated with susceptibility and eddy currents. Further, the fast heart rate in small animals allows only interleaved multi-shot EPI with very short echo train, which does not lead to significant improvement in imaging time. On the other hand, parallel imaging at high field is also limited by the general availability of phased array coils. As a result, it currently remains a challenge to apply EPI or parallel imaging for cardiac studies of small animals. Recently, we developed a saturation recovery Look-Locker (SRLL) method for fast T_1 mapping in mouse hearts at 160 s temporal resolution without the aid of

EPI or parallel imaging (59). However, this acquisition speed is still relatively slow compared with those accelerated by the fast imaging techniques (91, 107).

Compressed sensing (CS) has emerged as a promising fast imaging technique with fewer restrictions. By randomly under-sampling in the phase encoding (PE) direction, image acquisition can be greatly accelerated. The aliasing artifact can be effectively removed if the image or its transform domain can be sparsely represented by a few non-zero coefficients (109-111). The acceleration capability of CS has been successfully demonstrated in various applications, including angiography (110, 112), velocity encoding (113) and dynamic imaging (114, 115). Recently, Doneva et al also proposed a model-based CS method for fast MR parametric mapping (116, 117). This method was validated in simulated phantom and human brain with high SNR (116). However, a thorough evaluation of the factors that may impact the reconstruction accuracy is still lacking. Further, its feasibility in small animal imaging remains to be explored.

Small animal imaging, with the requirement for high spatial resolution, is often conducted at a higher magnetic field ($> 7T$) to maintain adequate SNR. Compared to similar studies on clinical scanners (1.5 or 3T), field inhomogeneity is much great at higher field strength because of the susceptibility difference. Hence, phase variation is more pronounced. Since model-based CS reconstruction relies on the physics of longitudinal relaxation that only describes the evolution of signal magnitude, the reconstruction of both magnitude and phase images is an underdetermined problem unless other constraints are imposed. In addition, with the constraint of fast acquisition, the signal-to-noise ratio (SNR) in small animal imaging is often limited due to the small voxel size, low average number and heart/respiration motion artifacts. The suboptimal SNR can considerably affect the

performance of the CS reconstruction. Therefore, the impact of SNR on the accuracy of CS-based T_1 mapping needs to be carefully evaluated.

In this study, we developed an approach that combined the model-based CS method with the SRLM method for fast cardiac T_1 mapping in small animals. Comprehensive evaluation was conducted to explore the accuracy and potential of this approach. Simulation studies were performed to evaluate the impact of imaging noise on reconstruction accuracy and the acceleration potential for high spatial-resolution imaging. In the phantom study, several approaches that provide pre-calculated phase maps for CS reconstruction were developed and evaluated to account for phase variations. Validation was performed in an *in vivo* cardiac manganese-enhanced MRI (MEMRI) study using mouse, which represented the most stringent experimental conditions.

4.2 Methods

4.2.1 Model-Based Compressed Sensing

Typically, CS accelerates the MR image acquisition by uniform random sampling in the PE direction. The missing signal can be reconstructed if the under-sampling is random. The resulting aliasing artifact is often removed by exploiting the sparsity of the images or their transform domain. A greater sparsity allows the achievement of higher degree of under-sampling, or the acceleration factor R .

In the case of MR parametric mapping, Doneva et al recently introduced a model-based compressed sensing method to exploit the sparsity along the parameter encoding direction for CS reconstruction (116). Briefly, for T_1 mapping using saturation recovery, the

signal, X_n , of a pixel from the n^{th} image acquired at time t_n after saturation preparation is governed by its T_1 , i.e.,

$$X_n = M_0(1 - \exp(-t_n / T_1)) \quad [1]$$

assuming each pixel has a single T_1 value. For a randomly under-sampled image series, the aliased signal X_n can be expressed as

$$X_n = M_0(1 - \exp(-t_n / T_1)) + B(1 - \exp(-t_n / T_{1,B})) + C(1 - \exp(-t_n / T_{1,C})) + \dots \quad [2]$$

where the coefficients (B, C, ...) of the aliasing terms are much smaller than that of the original one. In general, we can use the following transform to describe the signal evolution in a saturation recovery imaging series:

$$\begin{pmatrix} X_1 \\ \vdots \\ X_n \end{pmatrix} = D\gamma = \begin{pmatrix} 1 - \exp(-t_1 / T_{1,1}) & \dots & 1 - \exp(-t_1 / T_{1,m}) \\ \vdots & \ddots & \vdots \\ 1 - \exp(-t_n / T_{1,1}) & \dots & 1 - \exp(-t_n / T_{1,m}) \end{pmatrix} \begin{pmatrix} \gamma_1 \\ \vdots \\ \gamma_m \end{pmatrix} \quad [3]$$

where γ is the transform domain, and D is the transform matrix, also known as the dictionary (116). Each column in D , also referred to as an ‘atom’ (116), represented the signal model determined by a possible T_1 value of the pixel. To achieve sufficient precision in T_1 mapping, m is often a large number (>500) such that the dictionary contains all possible T_1 values of the imaging subject. In the case of a single T_1 value, the transform domain γ has only one non-zero coefficient out of m coefficients. Hence, sparsification of γ for the under-sampled images can effectively remove the aliasing artifact and thus allows accurate T_1 estimation.

In the current study, sparsification of γ was achieved by searching for the atoms that have the largest correlations with the signal series. Starting from the aliased images directly reconstructed from the under-sampled k-space data, CS reconstruction was performed iteratively until no improvement was achieved in the two consecutive iterations, i.e.,

$$\frac{\|X^{(i)} - X^{(i-1)}\|}{\|X^{(i)}\|} < \varepsilon$$

where $X^{(i)}$ was the reconstructed signal series at i^{th} iteration. The following steps were implemented in each iteration:

1. Decompose the signals into magnitude and phase;
2. Obtain the sparsified γ by performing a pixelwise greedy search using the orthogonal matching pursuit (OMP) algorithm (118) on magnitude image;
3. Use the sparsified γ to reconstruct the magnitude signal series, $|X^{(i)}|$;
4. Combine $|X^{(i)}|$ with the pre-calculated phase map to generate the complex signal series $X^{(i)}$;
5. Obtain the reconstructed k-space images by perform inverse Fourier transform on $X^{(i)}$;
6. Replace the reconstructed data with the originally acquired data at sampling locations, and Fourier transform the k-space images into the spatial domain.

4.2.2 Simulation Studies

To demonstrate the validity of the current model-based CS method, a digital Shepp-Logan phantom with T_1 values ranging from 0.3 to 1.5 s was used to simulate a T_1 mapping experiment. 30 images that covered 3.6 s of the saturation recovery process at a temporal resolution of 120 ms were generated using Eq.1 with a matrix size of 128x128. 2.5% Gaussian noises, which corresponded to a highest SNR of 40, were subsequently added to all images. The corresponding k-space images were then under-sampled with an acceleration factor of 2, 4, and 6 respectively. The 8 center PE lines were always fully sampled to maintain adequate SNR. The rest PE lines in the edge k-space were randomly sampled with equal probability for each line. A transform matrix, D , was generated with 581 atoms to cover T_1 values from 0.1 to 3 s. With 5 ms resolution, the atoms in the transform matrix

represented all T_1 values in the simulated phantom. The sparsity constraint, defined as the number of atoms used for reconstruction, was set to 1. The reconstructed images were fitted to yield pixelwise T_1 maps using in-house developed Matlab software (59). The root mean square error, normalized by the theoretical values, was used to quantify the deviation of the reconstructed images and T_1 maps from the theoretical noiseless ones.

To evaluate the accuracy of the current method at various experimental conditions, the Shepp-Logan phantom images were also generated with the addition of Gaussian noises that corresponded to SNR of 10 and 25. Under-sampling and reconstruction were performed as described above for each SNR. To evaluate the reconstruction accuracy of parameter alteration in small structures, mean T_1 values at focal regions with only 3-10 pixels were also compared with those in the theoretical noiseless T_1 map.

When acquiring images at high spatial resolution, data will cover a wider range in k space. Since high-frequency k-space data contain less power, a higher acceleration factor may be achieved. To evaluate the relationship between the acceleration power and the imaging resolution, the Shepp-Logan phantom images were generated in three matrix sizes, 128x128, 256x256, and 512x512, respectively. 64 PE lines were randomly acquired for all three groups, resulting in the same 'imaging' time but different acceleration factors of 2, 4 and 8, respectively. Image reconstruction and comparison were performed as described above.

4.2.3 Phantom Studies

The digital phantom used in the simulation study did not give rise to the phase variations that are present in real MRI images. To evaluate the robustness of the CS

reconstruction at the presence of phase variations, reconstructions were performed on MRI data acquired from a phantom tube filled with 300 μM MnCl_2 solution. T_1 measurement was performed on a horizontal 7T Bruker scanner (Bruker Biospin Co., Billerica, MA) using the saturation recovery Look-Locker (SRL) method (59) with the following imaging parameters: TR, 3 s; TE, 1.9 ms; number of averages, 1; number of fast low angle shot (FLASH) acquisitions, 20; image interval τ , 149 ms; slice thickness, 1 mm; field of view (FOV), $2 \times 2 \text{ cm}^2$; matrix size, 128×128 . A proton density image (M_0 image) required for T_1 calculation was acquired with the same imaging parameters prior to SRL acquisition (59). Two SRL datasets were acquired to evaluate the accuracy of using the phase maps of one fully-sampled dataset in the reconstruction of the other under-sampled dataset. Under-sampled images were retrospectively generated from the second dataset with an acceleration factor of 2. The sparsity constraint was set to 5 to simulate the imaging noise.

To account for the phase variations, phase maps were pre-calculated and incorporated in the CS reconstruction process. The pre-calculated phase maps were acquired using three different approaches. The first approach used the center 8 PE lines of the under-sampled images. The second approach used the phase map from the M_0 image. The third approach used the phase maps of a separate fully-sampled dataset that may represent a dataset acquired at the beginning or end of a dynamic contrast study. These phase correction methods were evaluated and compared with that without the use of pre-calculated phase maps.

The effective longitudinal relaxation time constant (T_1^*) that accounts for the partial saturation effect in Look-Locker acquisition was first obtained by performing pixel-wise single exponential curve fitting to the T_1 -weighted FLASH images. It was then combined with M_0 to calculate T_1 as described in our previous report (59).

4.2.4 In Vivo Studies

The accuracy and utility of the current method was further investigated in an *in vivo* manganese-enhanced MRI (MEMRI) study using a four month old C57BL/6 mouse. The animal was prepared as described previously (59). MR measurements were performed on the same scanner as the phantom study. A volume coil of 18 cm in length and 70 mm in diameter (Bruker, Billerica MA) was used as the transmitter coil. A 3-cm surface coil (Bruker, Billerica MA) was placed on the mouse chest and used as the receiver coil. The Mn^{2+} infusion protocol consisted of a 30-min intravenous injection of 126 mM MnCl_2 solution at a rate of 0.2 mL/h, followed by a 30-min washout period. The animal protocol was approved by the Institutional Animal Care and Use Committee of the Case Western Reserve University.

Short-axis T_1 maps were acquired using an ECG-triggered SRTL method (59) with the following imaging parameters: TE, 1.7 ms; TR, ~2500 ms; number of FLASH images, 9~12; image interval τ , 2 R-R interval ranging from 200 to 260 ms; flip angle, 10° ; slice thickness, 1.5 mm; FOV, $3 \times 3 \text{ cm}^2$. To evaluate the impact of SNR on reconstruction accuracy, the pre-contrast dataset was acquired with a 128×128 matrix size using one and two averages, respectively. Retrospective under-sampling was subsequently performed with an acceleration factor of 2. The phase map of the M_0 image was used for the reconstruction of the entire MEMRI datasets as the pre-calculated phase map. To demonstrate the validity of this approach, the M_0 phase map was compared with the phase maps of other fully-sampled SRTL images. The absolute difference in phase values at left ventricle was used for comparison. The reconstructed images were then fitted to generate T_1 maps as described previously (59). The resulting T_1 maps were compared with those obtained from fully

sampled datasets. The accuracy of reconstruction was assessed using the Bland-Altman plots. During the Mn^{2+} infusion period, the dynamic datasets were obtained with a 128x64 acquisition matrix size and one average to achieve a higher temporal resolution. Retrospective under-sampling and reconstruction was performed with an acceleration factor of 2. The resulting myocardial T_1 maps were compared with those obtained with fully sampled datasets at each time point.

To illustrate the application potential, the entire CS acquisition and reconstruction scheme was also implemented in a MEMRI study to track the dynamics of blood T_1 . M_0 was fully-sampled with a matrix size of 128x64 prior to Mn^{2+} injection. During the Mn^{2+} infusion period, a 128x32 under-sampling pattern was generated and implemented to reduce the imaging time to ~80 s. The under-sampled dataset was then reconstructed as described above. The T_1 of the blood in the left ventricular cavity was plotted against time to show the arterial input function.

4.2.5 Statistic Analysis

For comparison of image features, both visual and quantitative assessments were performed. Normalized root mean square error (NRMSE) was used to quantify the reconstruction error by calculating the pixelwise difference between the reconstructed images/maps and those obtained with fully sampling. For *in vivo* cardiac T_1 mapping, Bland-Altman plot (86) was used to evaluate the difference between the reconstructed and fully sampled datasets. Significant difference was assigned at a probability level < 5% ($p < 0.05$).

4.3 Results

The number of iterations was between 5 and 75 in the current study, depending on the SNR, acceleration factor, and matrix size. The computation time for each iteration was about 35s (Matlab, 2 GHz CPU and 3GByte RAM).

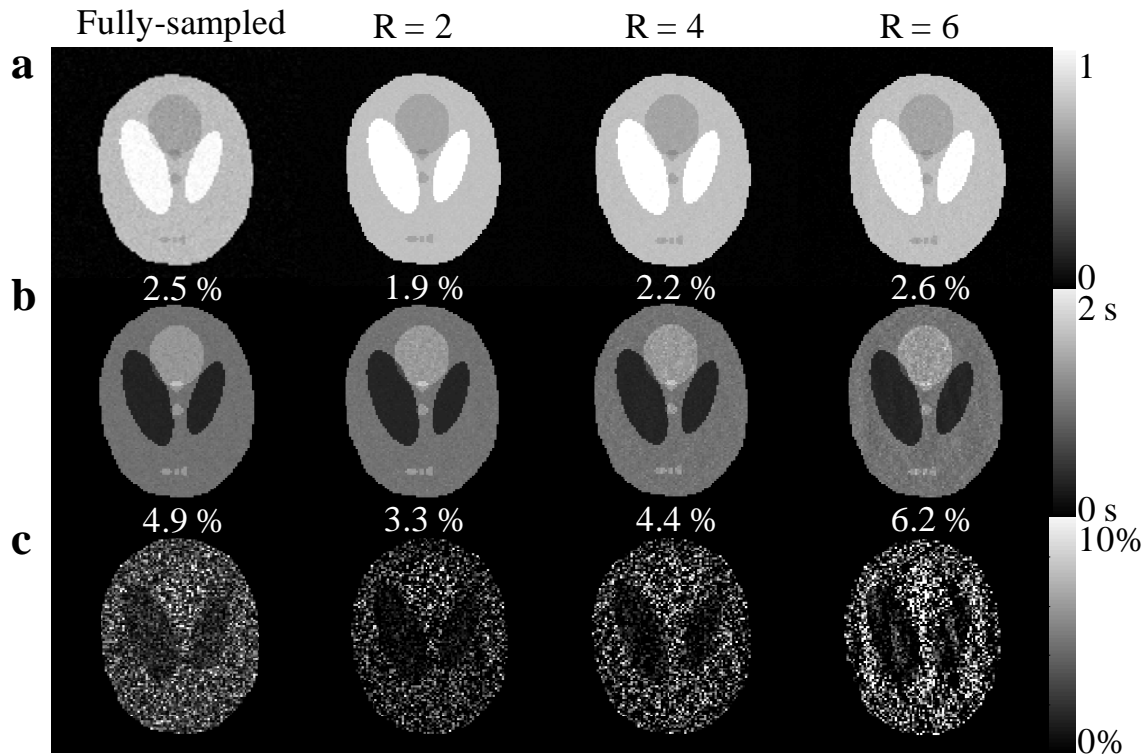


Figure 4.1 CS reconstruction of the Shepp-Logan phantom images simulated with different acceleration factors, R . **(a)** Reconstructed T_1 weighted images at $t = 1.5$ s after saturation preparation; **(b)** The resulting T_1 maps; **(c)** Difference maps between the reconstructed and the theoretical T_1 maps. The NRMSE is presented at the bottom of each image/map. The direction of phase encoding is from left to right.

4.3.1 Simulation Studies

Figure 4.1 shows the reconstructed images and the resulting T_1 maps generated from a digital phantom with an SNR of 40 and an acceleration factor of 2, 4, and 6, respectively. Although the reconstruction error increased slightly with the acceleration factor, it remained

small and random. Regions with shorter T_1 values had higher SNR and consequently smaller reconstruction errors. For the fully sampled dataset, the 2.5% Gaussian noise led to a NRMSE of 4.9% in the calculated T_1 map, which was greater than that with an acceleration factor of 2 or 4. This suggests that the CS reconstruction allowed the removal of both Gaussian and aliasing artifacts. Figure 4.2 further shows the reconstructed T_1 maps with different matrix sizes and acceleration factors. At the same SNR, a higher acceleration factor can be achieved with a larger matrix without compromising the accuracy of T_1 estimation. These results demonstrate the validity of the current model-based CS method.

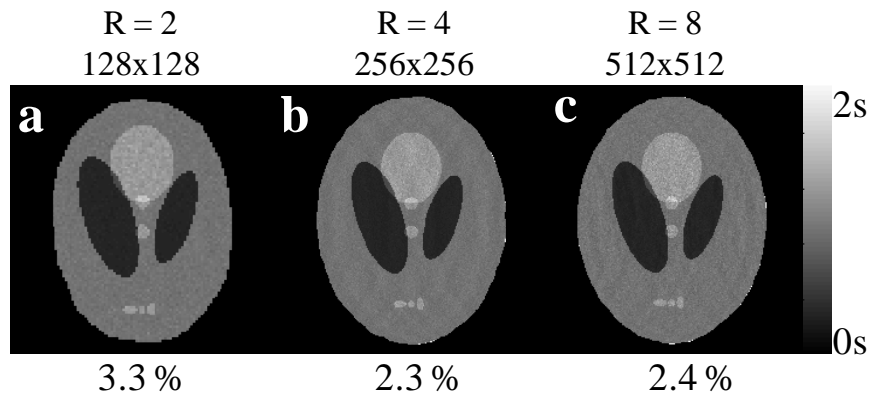


Figure 4.2 CS reconstructed T_1 maps at different spatial resolution. Acceleration factors of 2, 4 and 8 were employed to under-sample k-space images with a matrix size of **(a)** 128x128; **(b)** 256x256, and **(c)** 512x512, respectively. The NRMSE is presented at the bottom of each T_1 map. The direction of phase encoding is from left to right.

Figure 4.3 shows the impact of SNR on reconstruction accuracy. Although the current method can partially remove the Gaussian noises, the reconstruction error increased sharply with decreased SNR (Fig. 4.3a). With an SNR of 10, the NRMSE was above 12% even at the lowest acceleration factor of 2. Nevertheless, with a moderate SNR of 25, the reconstruction error was only slightly increased from that with an SNR of 40.

The reconstruction accuracy was further evaluated by examining the variations of reconstructed T_1 values in fine structures (Fig. 4.3b-e). In general, the variations of normalized T_1 difference increased with the acceleration factor and noise level. With an SNR higher than 25, the variations were always within 20%. At a low SNR of 10 or high acceleration factor of 6, pixels showing large ($\sim 40\%$) deviations from the theoretical T_1 values were present. On the other hand, the mean T_1 values remained close to the theoretical ones under all conditions. For regions containing more than 6 pixels, the mean difference with respect to the theoretical T_1 values was always below 5% when SNR was above 10. For the region with only 3 pixels, the difference was generally greater. Nevertheless, the largest difference in mean T_1 values remained $<15\%$ when both the high acceleration factor and low SNR conditions were present. These results suggest that an accurate estimation of the mean regional T_1 values can be achieved even at high acceleration factors.

4.3.2 Phantom Studies

Figure 4.4 compares the results of different reconstruction approaches using MRI data acquired from a phantom with homogenous T_1 values. Without using a pre-calculated phase map, large reconstruction errors were present as a result of noise-induced phase variations (Fig. 4.4a&e). Using the low-resolution phase maps generated from the center 8 PE lines, the reconstruction error was greatly reduced. However, aliasing artifacts remained noticeable in the reconstructed T_1 map (Fig. 4.4b&f). These artifacts were completely removed when high-resolution phase maps were obtained from either the M_0 image or a separate fully sampled dataset (Fig. 4.4c&d).

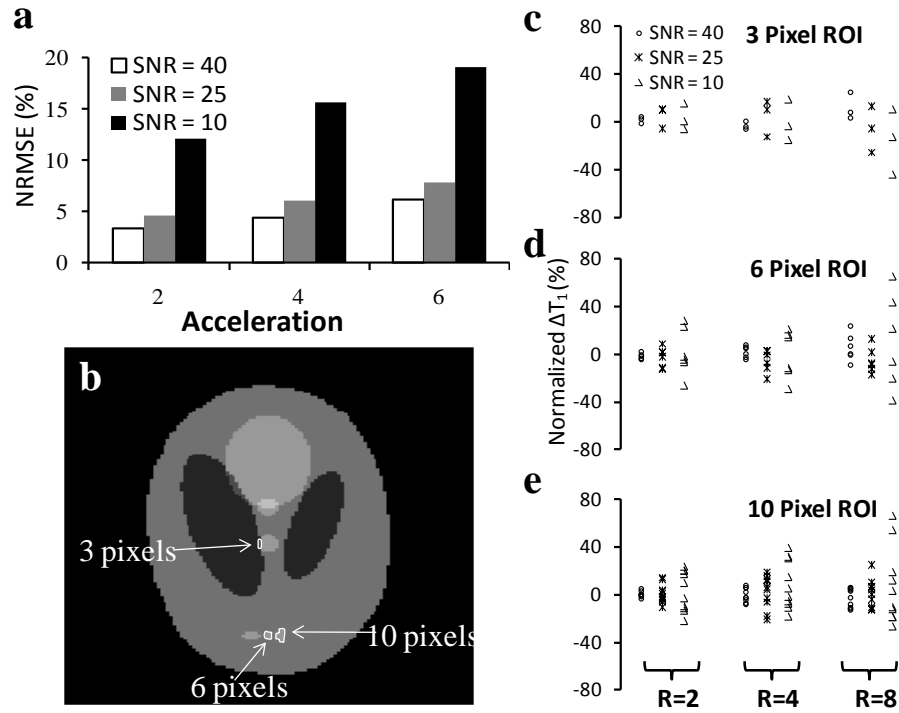


Figure 4.3 The impact of SNR and high spatial-frequency structures on CS reconstruction. **(a)** The NRMSE of the reconstructed T_1 maps at different SNR; **(b)** Theoretical T_1 map showing focal regions with different pixel numbers; **(c)-(e)** Pixel-wise differences between the theoretical and CS estimated T_1 values in the regions outlined in **(b)**.

4.3.3 *In Vivo* Studies

Fig. 4.5 demonstrates the validity of using M_0 image for phase estimation. Large phase variations were observed in the M_0 image (Fig. 4.5a), suggesting the necessity of phase estimation for CS reconstruction. Pixelwise comparison of the phase in M_0 image and in SRLL images showed strong agreement between the two (Fig. 4.5b-d). The few outliers occurred around 0° or 180° due to phase wrapping. Average difference in phase values was less than 5° between the M_0 image and all SRLL images. These results suggest the validity of using the M_0 image to pre-calculate phase maps for CS reconstruction of the entire MEMRI dataset.

Figure 4.6 shows the selected CS reconstruction results of an *in vivo* T_1 mapping study in mouse heart. At an acceleration factor of 2, the aliasing artifact induced by under-sampling was successfully removed using pre-calculated phase map from the M_0 image (Fig. 4.6e-h). The mean myocardial T_1 value in the reconstructed dataset was the same as that obtained from the fully sampled dataset (Fig. 4.6i&j). The standard deviation (SD) of the difference was also small (<14 %). While these results were from dataset acquired with two averages, similar reconstruction accuracy was also observed for dataset acquired with one average. The difference of the mean T_1 values fitted from the fully sampled and CS reconstructed datasets was only 2.6%. These results suggest that the current CS method can shorten the acquisition time by at least 50% without reducing the accuracy and spatial resolution for T_1 estimation.

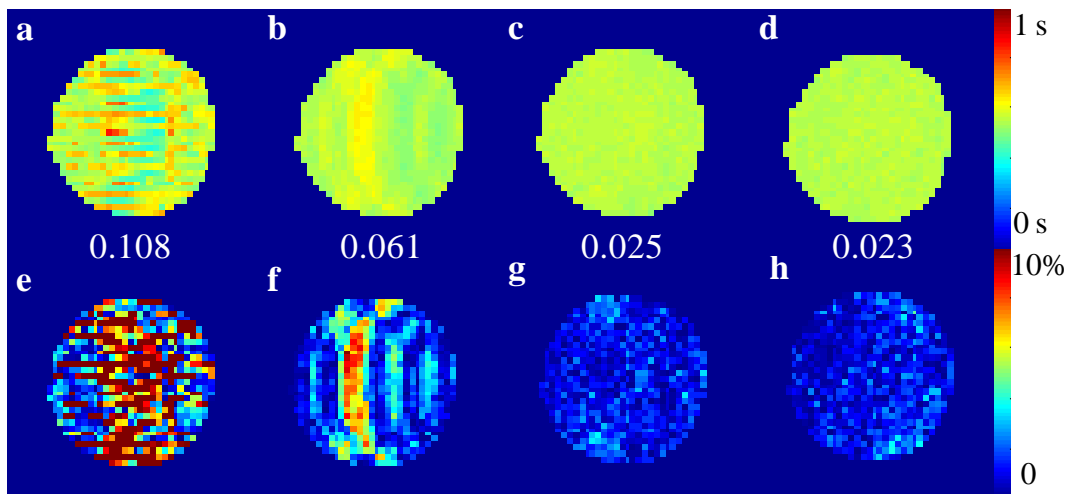


Figure 4.4 Impact of using phase maps for CS reconstruction. The direction of phase encoding is from left to right. **(a)-(d)** Reconstructed T_1 maps without using a pre-calculated phase map (a) and using the phase maps calculated from the 8 center PE lines (b), the fully sampled M_0 image (c), and a separate fully sampled T_1 mapping dataset (d), respectively. The NRMSE is presented at the bottom of each T_1 map. **(e)-(h)** Corresponding difference images of the fully sampled and CS reconstructed T_1 maps.

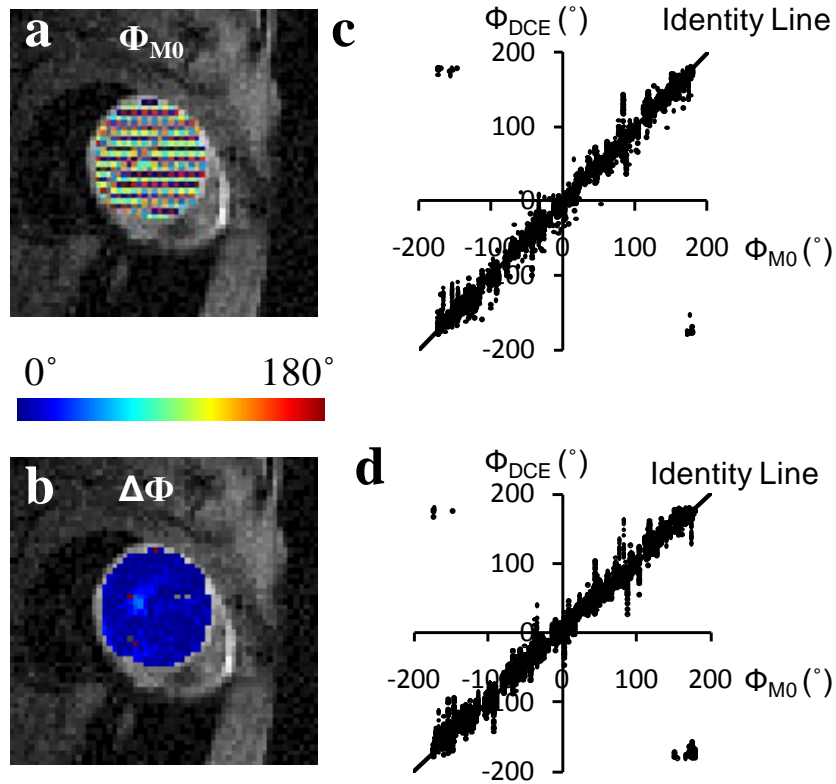


Figure 4.5 Phase map of the *in vivo* mouse heart. **(a)** Phase map of the M_0 image. **(b)** Absolute difference in phase values between the M_0 image and a SRL image acquired at baseline. **(c)&(d)** Phase values of the M_0 image versus phase values of **(c)** all SRL images acquired at baseline and **(d)** every ninth SRL images in the T_1 datasets acquired during the entire MEMRI period.

The myocardial T_1 values from CS reconstructed images were in good agreement with those obtained with full k-space sampling at all time points (Fig. 4.6k). The largest difference, occurred at 15 min post-injection, was only 0.05 s. As a result, the two T_1 dynamic curves largely overlapped during the entire Mn^{2+} imaging protocol. Using the current CS method, the acquisition time for each T_1 map can be reduced from 160 s to 80 s while maintaining the high spatial resolution of $234 \times 469 \mu m^2$.

4.4 Discussion

We have presented a robust fast T_1 mapping method for small animal imaging by combining a modified model-based CS method (116) and SRLM method (59). By incorporating the pre-estimated phase information in the CS reconstruction process, the aliasing artifact caused by under-sampling can be effectively removed. The performance of the CS method was evaluated at various experimental conditions in both simulation and MRI studies. A 50% reduction in imaging time can be achieved for *in vivo* T_1 mapping of mouse heart. Since both EPI and parallel imaging have limitations at high field, this model-based CS method provides a unique approach to fast T_1 mapping in small animals.

Similar to parallel imaging, SNR was found to be an important determinant of the accuracy of the current CS method. With low SNR, the noise diminishes the signal dominance from the unaliased pixels. As a result, sparsification may yield similar coefficients for the unaliased and aliased pixels, leading to inaccurate reconstruction. Nevertheless, an SNR of 20, which is considered as the acceptable level in most MRI studies, was demonstrated to be adequate for accurate CS reconstructions in our studies.

With an SNR at this level, higher acceleration factors can be achieved for acquisition of images with higher spatial resolution and larger matrix size. The high acceleration capability is mainly because the energy spectrum of an image is mostly concentrated in the low-frequency region. Hence, sampling the same number of center PE lines as in the acquisition of low resolution images is sufficient to capture the majority of the dynamic changes in signals. In the meantime, multi-acquisition along the magnetization recovery curve allows each high-frequency PE line to be sampled several times in the entire dataset. Our results suggest that similar accuracy can be achieved at greater acceleration factors with

such a sampling scheme of the high spatial-frequency region (Fig. 4.2). The high acceleration factor in acquiring high-resolution images can have enormous benefit in saving imaging time. Without any under-sampling, doubling the spatial resolution in two dimensions needs a 16-fold increase in imaging time to achieve the same SNR. With CS under-sampling and reconstruction, only a 4-fold increase in imaging time is needed (Fig. 4.2).

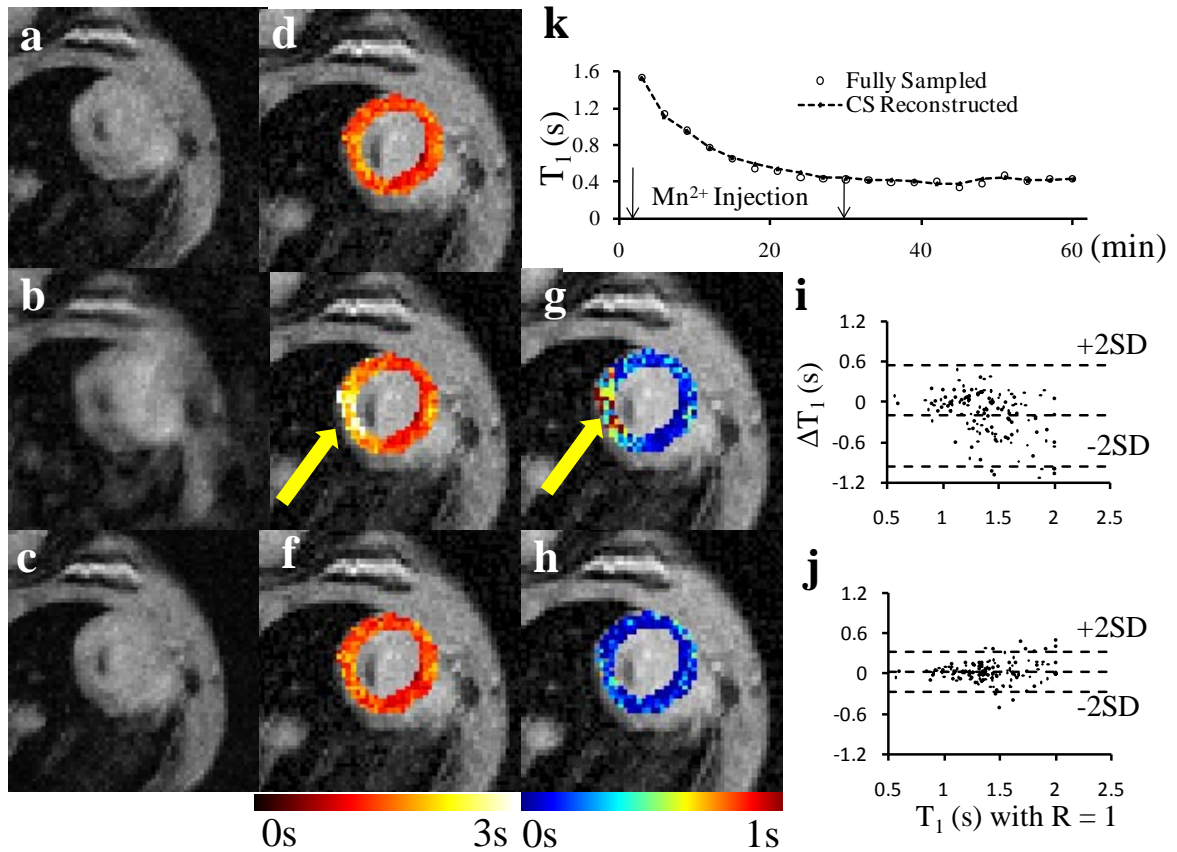


Figure 4.6 *In vivo* MEMRI study of the mouse heart. (a) T_1 weighted image acquired with full sampling at 1.5 s after saturation preparation; (b) reconstructed under-sampled image using zero-padding; (c) CS reconstructed under-sampled image; (d)-(f) The corresponding T_1 maps; (g)&(h) The corresponding differences maps of T_1 ; (i)&(j) Bland-Altman plots showing the difference in T_1 values estimated from the fully-sampled dataset and under-sampled dataset (i) or CS reconstructed dataset (j); (k) Time courses of the average myocardial T_1 values during the contrast infusion period. The direction of phase encoding is from left to right. Yellow arrows indicate the aliasing artifact.

In real life, phase variations are always present in images as a result of hardware imperfection and subject inhomogeneity. However, the sparsifying transform in the current study used a model that describes only the magnitude of the signal recovery. As a result, aliasing of the phase values cannot be effectively removed. Since phase is an important component of the MRI signal, correct reconstruction of the phase values is critical for the convergence and accuracy of image reconstruction (109-111, 113, 115, 119, 120). A previous study used fully sampled center PE lines to generate a low-resolution phase map for the reconstruction (110). However, such approach does not account for contributions to phase map from the high spatial-frequency regions. In the current study, the fully sampled center PE lines only comprised of <7 % of the entire k space. We found such an approach cannot completely remove the aliasing artifact (Fig. 4.5b). Alternatively, since phase variations are largely caused by field inhomogeneity, images acquired with the same triggered pulse sequence have similar phase maps (Fig. 4.5b-d). Hence, a high-resolution phase map obtained from a fully sampled image prior to CS acquisition should improve the reconstruction. T_1 mapping using the SRLM method requires the acquisition of the proton density image, or the M_0 image. This M_0 image can be fully sampled prior to the SRLM scan (59). It is also of high SNR as there is no signal loss caused by T_1/T_2 weighting. Therefore, its phase map can be used in the CS reconstruction. Alternatively, for dynamic contrast MRI studies, the phase maps can also be obtained by fully sampling the baseline dataset prior to the introduction of contrast agent. Our study showed that both approaches allowed accurate reconstruction of the T_1 maps in mouse heart (Fig. 4.6).

The accuracy of T_1 estimation in the current method is governed by the resolution of the dictionary. If the true T_1 value is not included in the dictionary, the reconstruction will

yield the closest T_1 value in the dictionary. Therefore, a large range of T_1 values with high resolution is desired for the construction of dictionary. However, the computation time is proportional to the number of atoms in the dictionary. Thus, a compromise is often made to balance the accuracy and the computation time. In the current study, the dictionary was constructed using T_1 values ranging from 100 to 3000 ms with 5 ms resolution. Given that the shortest T_1 value upon Mn^{2+} injection was ~ 400 ms, the estimation error of using this dictionary was less than 0.6% with a reasonable computation time (35 s per iteration).

In the current CS reconstruction method, each pixel is assumed to have a single T_1 value, which can be a lumped value from multiple cellular components. It is possible to fit multiple T_1 values by modifying the signal model of the CS reconstruction. However, similar to the fitting from a fully-sampled dataset, additional unknown parameters will result in increased fitting uncertainty if a two-/multi-compartment model is used in the CS reconstruction. Therefore, a careful and thorough evaluation is needed before applying the current CS method to two-/multi-compartment models.

The current study used a uniform under-sampling pattern to provide a good coverage of the high spatial-frequency regions. The reconstruction accuracy was comparable to that of the commonly used variable density sampling pattern with sampling probability inversely proportional to the distance from the center PE line (110). However, it is not clear whether further improvement can be achieved by using other under-sampling schemes. The Monte-Carlo design procedure (110) may be helpful to gain better insights of this issue. Further, while the current work focused on T_1 mapping, this model-based CS approach can be readily extended to the measurement of other MR parameters such as diffusion coefficients. In addition, the compatibility of the CS method with parallel imaging has been demonstrated in

several reports (110, 120-122). Therefore, a combination of the current CS method with parallel imaging holds great potential to achieve even higher acceleration factors for MR parametric mappings.

Chapter 5 A Two-Compartment Kinetic Model for Quantification of Ca^{2+} Cycling

5.1 Introduction

Kinetic modeling is increasingly used in DCE-MRI studies to provide quantitative delineation of the physiological parameters, i.e., blood vessel permeability, extracellular volume fraction (38, 41, 42). Currently, many types of compartment models have been developed to describe the Gd-based contrast agent distribution in intravascular and extracellular spaces (38, 39, 123). On the contrary, few models have been developed to describe Mn^{2+} dynamics. Since Mn^{2+} can also cross cell membrane, a two compartment model that includes the intracellular space is needed. The additional compartment increases the number of unknown parameters and presents higher requirement on the accuracy of the experimental data.

Up to date, only one attempt has been made by Skjold et al. In this study, a two compartment model was combined with qualitative MEMRI measurement to estimate Ca^{2+} influx rate across the cell membrane (8). The apparent unidirectional influx constant was consistent for two different infusion protocols, suggesting the validity of the measurement and modeling analysis. However, other rate constants and extracellular volume were inconsistent with their physiological conditions, which degrade the reliability of the modeling analysis. Besides the errors introduced in the data acquisition step, the unrealistic assumptions in the model may account for this inconsistency. For example, the relaxivity of Mn^{2+} in blood and myocardium was assumed to be the same, while they may be different (7, 31). The zero efflux rate assumed in the study was also found to have a small value in

previous report (7). Therefore, further development and validation of a two compartment model is needed.

In the current study, a two compartment model was developed and validated using quantitative MEMRI datasets. Sensitivity analysis was performed first to evaluate the robustness of the model (124). *Ex vivo* MRI perfusion studies were then performed for validation. Ca^{2+} influx rates were varied by manipulating ingredients in the perfusion buffer. The expected Ca^{2+} influx rates were then compared with those obtained from the model estimated values to validate the robustness of the MEMRI measurement and modeling analysis.

5.2 Methods

5.2.1 Two-Compartment Kinetic Model

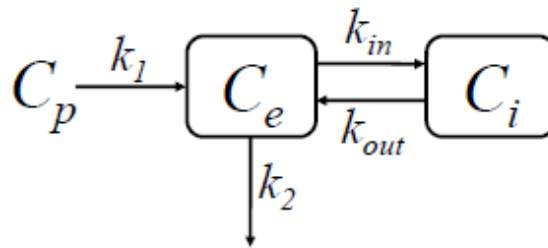


Figure 5.1 Two compartment model for Mn^{2+} dynamics.

A two compartment model was developed in Matlab to delineate the Mn^{2+} kinetics across different cellular compartments (Fig.5.1). k_1 , k_2 , k_{in} and k_{out} are the transfer rate constants in the unit of min^{-1} . k_1 was set to equal to k_2 since the diffusion coefficient across the same blood vessel wall should be the same. Because of the strong coupling between k_1 and k_{in} , a lumped rate constant k_i calculated as $k_1 * k_{in} / (k_1 + k_{in})$ was used to indicate the

overall influx rate (8, 125). C_p , C_e and C_{in} represent the Mn^{2+} concentration (μM) in capillary, extracellular and intracellular compartments, respectively. The sum of Mn^{2+} content in all compartments, C_{tot} , was converted from the myocardial R_1 measured in MRI studies. For the current perfusion study, C_p was a step function with 30 μM during the 30 min infusion period and zero at other times. For *in vivo* studies, it can be converted from blood R_1 measurement. The dynamics of Mn^{2+} distribution in each compartment were described by:

$$\frac{dC_e(t)}{dt} = k_1 * C_p(t) - (k_2 + k_{in}) * C_e(t) + k_{out} * C_i(t) \dots \dots \dots [5.1]$$

$$\frac{dC_i(t)}{dt} = k_{in} * C_e(t) - k_{out} * C_i(t) \dots \dots \dots [5.2]$$

$$C_{tot}(t) = (C_e(t) + C_{in}(t)) * (1 - BV) + BV * C_p(t) \dots \dots \dots [5.3]$$

BV represents the fractional volume of blood vessels in each image pixel and was set to 0.09 according to the literature (123).

5.2.2 Perfusion MEMRI Experiment Design

8-10 weeks male Sprague-Dawley rats were heparinized (100IU IP) and anesthetized by sodium pentobarbital (85 mg/kg IP). The heart was excised, cannulated, and perfused with Krebs-Henseleit (KH) buffer containing (in mM) 118.5 NaCl, 4.7 KCl, 1.2 $MgSO_4$, 1.2 KH_2PO_4 , 1.5~2.5 $CaCl_2$, 11.1 glucose, 25 $NaHCO_3$. The perfusate was maintained at 37°C and equilibrated with 95% O_2 - 5% CO_2 . A water-filled latex balloon was inserted into the left ventricle and connected to a pressure transducer to record the left ventricular pressure and heart rate. The rate-pressure product (RPP), i.e., the product of left ventricle developed pressure (LVDP) and the heart rate (HR), was calculated as an index of the workload.

There were three experimental groups: 1) hearts perfused with 1.5 mM Ca^{2+} under normal workload; 2) hearts perfused with 0.5 μM isoproterenol (ISO) to induce β -adrenergic stimulation; 3) hearts perfused with 2.5 mM Ca^{2+} to increase the workload without altering the L-type Ca^{2+} channel activity. The heart was paced at 480 bpm during β -adrenergic stimulation and at 360 bpm at other conditions. Once the heart rate and pressure were stabilized, the perfusate was switched to modified KH buffer containing 30 μM MnCl_2 for 30 min (the wash-in period), followed by 30 min washout period with Mn^{2+} -free buffer. In the modified KH buffer, the phosphate and sulfate were replaced with chloride to prevent Mn^{2+} precipitation. At the end of imaging acquisition, hearts were frozen in liquid nitrogen for tissue analysis.

The imaging was performed on a 9.4T vertical Bruker scanner (Bruker Biospin, Billerica, MA) with a 20-mm birdcage RF coil (Bruker Biospin, Billerica, MA). The electric signal that used to pace the heart was sent to the MRI control unit as the ECG signal to trigger image acquisitions. T_1 maps of a short-axis slice at mid-ventricle were continuously acquired using triggered SRTL at baseline and during the 30 min Mn^{2+} infusion and washout periods. The imaging parameters were as follows: TE, 1.7 ms; TR, ~ 2.6 s; τ , 166/125 ms at baseline/stimulated conditions; Image Numbers, 16/20 at baseline/stimulated conditions; flip angle, 10° ; slice thickness, 1 mm; number of averages, 1; FOV, 3×3 cm^2 ; matrix size, 128×64 ; Images were zero-filled to 128×128 during reconstruction. The acquisition time of each T_1 map was 3 min. During data processing, the T_1 values myocardium were obtained by pixel-wise fitting of the signal intensities to the SRTL signal model as described previously (59).

5.2.3 Model Validation

To evaluate the robustness of the model, a sensitivity analysis was first performed using the perfusion dataset with 1.5 mM Ca^{2+} concentration. A pilot fit was performed to obtain the values of k_1 , k_{in} and k_{out} . Each parameter was then varied over a wide range with the other two parameters fixed at the pre-estimated value. The objective function values were calculated and plotted against the varying parameters to show the effects of each parameter on model output.

To evaluate the validity of the model, the perfusion datasets with different Ca^{2+} concentrations and inotropic states were analyzed using the current model, respectively. The estimated Ca^{2+} influx rate constants k_i was compared with the anticipated Ca^{2+} influx rate. Other model fitted parameters such as k_{out} were also evaluated to further demonstrate the validity of the current model.

5.3 Results and Conclusion

Fig. 5.2 shows the results of the sensitivity analysis. The value of the objective function was a convex function with distinct global minimum for all three rate constants. In addition, the changes in objective function value were steep near the global minimum point. These results suggest that the parameters estimated from the model are sensitive to variations contained in the experimental data.

Fig. 5.3 shows that the Mn^{2+} flux rates fitted by the current model were in good agreement with the expected Ca^{2+} influx rates. Specifically, similar Mn^{2+} influx rates were found in the groups perfused with buffers containing 1.5 and 2.5 mM Ca^{2+} concentrations, respectively. This is consistent with the expected unvarying Ca^{2+} influx rate since the

voltage gated Ca^{2+} channel activity is independent of extracellular Ca^{2+} concentration. In the ISO group with positive inotropic state, the elevated L-type Ca^{2+} channels activity was faithfully reflected by the significantly increased Mn^{2+} influx rate. On the other hand, the Mn^{2+} efflux rate, k_{out} , was small for all groups, which is consistent with the long intracellular retention time of Mn^{2+} (4).

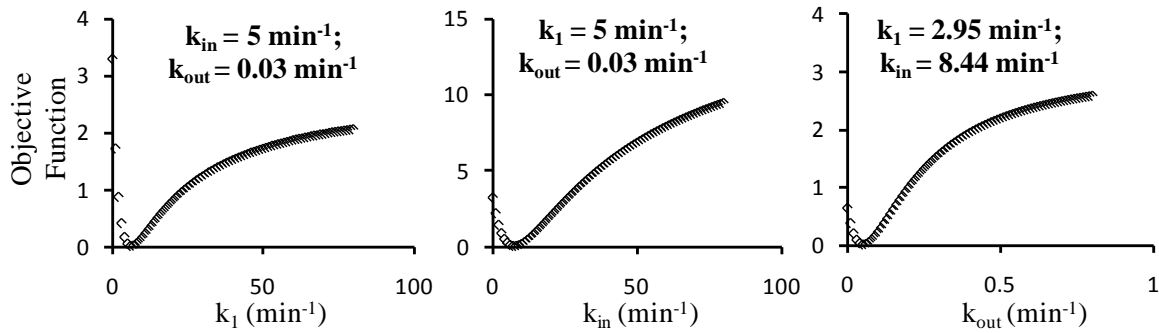


Figure 5.2 Sensitivity analysis of the MEMRI model.

In conclusion, the consistency between the model fitted parameters and the actual physiological conditions demonstrate the robustness of the current MEMRI measurements and kinetic modeling analysis for quantification of *in vivo* Ca^{2+} influx rate and L-type Ca^{2+} channel activities.

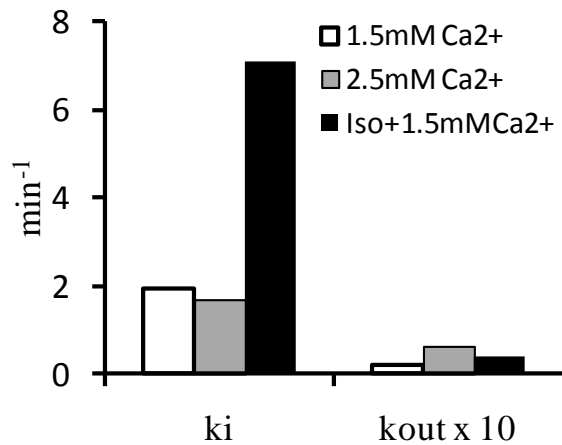


Figure 5.3 Model fitted Mn^{2+} influx and efflux rates for the perfusion MEMRI datasets.

Chapter 6 Conclusion and Future Directions

6.1 Conclusion

In the current thesis project, we established a quantitative MEMRI method for accurate evaluation of *in vivo* L-type Ca^{2+} channel activity in small animals. The sensitivity of MEMRI to subtle Ca^{2+} influx alterations was demonstrated in a transgenic mouse model, which significantly expanded the application scope of MEMRI. Fast cardiac T_1 mapping techniques were developed and validated to provide accurate measurement of the dynamic dataset. A saturation recovery Look-Locker method was first developed. By sampling only a portion of the longitudinal recovery curve for T_1 fitting, imaging time was reduced by more than 60% compared with the gold-standard inversion recovery Look-Locker method. A model-based compressed sensing method was subsequently developed to further expedite T_1 mapping. By innovatively incorporating the pre-estimated phase information into the CS reconstruction, an acceleration factor of 2 was successfully achieved for *in vivo* T_1 mapping of mouse heart. The combination of the CS and SRTL method allows simultaneous T_1 mapping of both myocardium and blood at a high spatial resolution of $234 \times 469 \mu\text{m}^2$ within 80 s. Finally, a two-compartment kinetic model was developed to extract $\text{Mn}^{2+}/\text{Ca}^{2+}$ flux rates. The fast T_1 mapping method was applied in perfusion MEMRI studies with Ca^{2+} influx rates well controlled by buffer ingredients. The model-fitted $\text{Mn}^{2+}/\text{Ca}^{2+}$ flux rates were in good agreement with the expected physiological conditions.

The accomplishment of this study not only provides a powerful tool for *in vivo* assessment of the L-type Ca^{2+} channel activity, but may also be readily extended to evaluate the Ca^{2+} efflux mechanisms. In addition, the fast T_1 mapping techniques developed in the current study can be applied to provide quantitative data acquisition in all kinds of DCE-MRI

studies. The model-based compressed sensing method may also be readily translated to accelerate the measurements of T_2 and diffusion coefficients.

6.2 Future Directions

6.2.1 Evaluation of Ca^{2+} Efflux Rate with MEMRI

Compared to abnormal Ca^{2+} influx, an imbalanced intracellular Ca^{2+} transient is more commonly presented in pathological conditions (4, 126). Therefore, a robust evaluation of both Ca^{2+} influx and efflux rates will further enhance the diagnosis power of MEMRI. Waghorn et al explored along this direction by correlating the Mn^{2+} efflux changes with the activity of the Na^+/Ca^{2+} exchanger (NCX), a major exit route for Ca^{2+} (127-129). The model fitted Mn^{2+} efflux rate was significantly reduced with NCX inhibition, suggesting that MEMRI is also sensitive to NCX activity (7). However, a complete understanding of the Mn^{2+} efflux mechanism remains lacking. The presence of any other Mn^{2+} efflux route may bias the estimation. In addition, the efflux rate of Mn^{2+} across sarcolemma may also be affected by its compartmentalization within the cell, i.e., mitochondria. Although most intracellular Mn^{2+} are suggested to be in free state (7), a thorough evaluation remains lacking. Therefore, to expand the application of current MEMRI method to evaluating the entire Ca^{2+} cycling process, an important direction of future developments is to elucidate the efflux mechanism of intracellular Mn^{2+} .

6.2.2 Development of Standardized DCE-MRI

The quantitative data acquisition approach developed in the current project can also have a significant impact on other DCE-MRI studies. The quantitative analysis offers the

potential to develop standardized DCE-MRI protocols for multi-center and multi-trial studies, which will greatly improve the accuracy of DCE-MRI analysis and expand its applications to clinical phase II and III trials. Therefore, a promising future direction is to explore the application potential of the current quantitative DCE-MRI method in different fields, i.e., cancer studies and cardiac studies.

Technical developments may also be performed to improve the sampling speed once the imaging requirement loosens in specific applications. For example, without the constraints from ECG-triggering, the sampling number (FLASH images) along the longitudinal recovery curve can be greatly increased when imaging static tissues, i.e., brain and knees. The increased sampling points will improve the accuracy of T_1 fitting. It may also allow a greater acceleration factor using the model-based CS method since the sparsity is promoted. Nevertheless, these promising potentials need to be carefully evaluated on a case-by-case basis.

6.2.3 Translating MEMRI Method to Clinical Practices

The ultimate goal of the current thesis project is to make quantitative MEMRI diagnosis in clinical settings. The quantification of *in vivo* Ca^{2+} influx rate can benefit the diagnosis and treatment evaluation in many ways. For example, it can individualize the treatment evaluation of Ca^{2+} blocker, which is commonly applied to decrease blood pressure, control heart rate and prevent cerebral vasospasm in clinical practices. It may also be used for prognosis of hypertension, which is a major risk factor for stroke and myocardial infarction (130).

In summary, although the application was only demonstrated in small animals, the current work lays the cornerstone for future applications of MEMRI to diagnosis and treatment evaluation of patients with disturbed Ca^{2+} homeostasis. The methods developed in the current study also provide invaluable tools to achieve quantitative analysis in all types of DCE-MRI studies.

Bibliography

1. SANDOW A. Excitation-contraction coupling in muscular response. *Yale J Biol Med* 1952;25(3):176-201.
2. Mongillo M. Models of heart failure progression: Ca²⁺ dysregulation. *Drug Discovery Today: Disease Models* 2009;4(4):191-196.
3. Seidler T, Hasenfuss G, Maier LS. Targeting altered calcium physiology in the heart: translational approaches to excitation, contraction, and transcription. *Physiology (Bethesda)* 2007;22:328-334.
4. Hunter DR, Haworth RA, Berkoff HA. Cellular manganese uptake by the isolated perfused rat heart: a probe for the sarcolemma calcium channel. *J Mol Cell Cardiol* 1981;13(9):823-832.
5. Vernino S, Rogers M, Radcliffe KA, Dani JA. Quantitative measurement of calcium flux through muscle and neuronal nicotinic acetylcholine receptors. *J Neurosci* 1994;14(9):5514-5524.
6. Hu TC, Pautler RG, MacGowan GA, Koretsky AP. Manganese-enhanced MRI of mouse heart during changes in inotropy. *Magn Reson Med* 2001;46(5):884-890.
7. Waghorn B, Yang Y, Baba A, Matsuda T, Schumacher A, Yanasak N, Hu TC. Assessing manganese efflux using SEA0400 and cardiac T1-mapping manganese-enhanced MRI in a murine model. *NMR Biomed* 2009;22(8):874-881.
8. Skjold A, Kristoffersen A, Vangberg TR, Haraldseth O, Jynge P, Larsson HB. An apparent unidirectional influx constant for manganese as a measure of myocardial calcium channel activity. *J Magn Reson Imaging* 2006;24(5):1047-1055.

9. Lauterbur PC. Image formation by induced local interactions. Examples employing nuclear magnetic resonance. 1973. Clin Orthop Relat Res 1989;(244):3-6.
10. Kirsch JE. Basic principles of magnetic resonance contrast agents. Top Magn Reson Imaging 1991;3(2):1-18.
11. Nelson KL, Runge VM. Basic principles of MR contrast. Top Magn Reson Imaging 1995;7(3):124-136.
12. MILDVAN AS, COHN M. MAGNETIC RESONANCE STUDIES OF THE INTERACTION OF THE MANGANOUS ION WITH BOVINE SERUM ALBUMIN. Biochemistry 1963;2:910-919.
13. EISINGER J, FAWAZ-ESTRUP F, SHULMAN RG. BINDING OF Mn^{2+} TO NUCLEIC ACIDS. J Chem Phys 1965;42:43-53.
14. Fabry ME, Eisenstadt M. Water exchange between red cells and plasma. Measurement by nuclear magnetic relaxation. Biophys J 1975;15(11):1101-1110.
15. Koretsky AP, Silva AC. Manganese-enhanced magnetic resonance imaging (MEMRI). NMR Biomed 2004;17(8):527-531.
16. Silva AC, Lee JH, Aoki I, Koretsky AP. Manganese-enhanced magnetic resonance imaging (MEMRI): methodological and practical considerations. NMR Biomed 2004;17(8):532-543.
17. Pautler RG, Koretsky AP. Tracing odor-induced activation in the olfactory bulbs of mice using manganese-enhanced magnetic resonance imaging. Neuroimage 2002;16(2):441-448.

18. Pautler RG, Silva AC, Koretsky AP. In vivo neuronal tract tracing using manganese-enhanced magnetic resonance imaging. *Magn Reson Med* 1998;40(5):740-748.
19. Allegrini PR, Wiessner C. Three-dimensional MRI of cerebral projections in rat brain in vivo after intracortical injection of MnCl₂. *NMR Biomed* 2003;16(5):252-256.
20. Watanabe T, Radulovic J, Boretius S, Frahm J, Michaelis T. Mapping of the habenulo-interpeduncular pathway in living mice using manganese-enhanced 3D MRI. *Magn Reson Imaging* 2006;24(3):209-215.
21. Natt O, Watanabe T, Boretius S, Radulovic J, Frahm J, Michaelis T. High-resolution 3D MRI of mouse brain reveals small cerebral structures in vivo. *J Neurosci Methods* 2002;120(2):203-209.
22. Aoki I, Wu YJ, Silva AC, Lynch RM, Koretsky AP. In vivo detection of neuroarchitecture in the rodent brain using manganese-enhanced MRI. *Neuroimage* 2004;22(3):1046-1059.
23. Shannon RD. Revised effective ionic radii and systematic studies of interatomic distances in halides and chalcogenides. *Acta Crystallographica Section A* 1976;32:751-767.
24. Takeda A. Manganese action in brain function. *Brain Res Brain Res Rev* 2003;41(1):79-87.
25. Silva AC, Bock NA. Manganese-enhanced MRI: an exceptional tool in translational neuroimaging. *Schizophr Bull* 2008;34(4):595-604.

26. Hu TC, Christian TF, Aletras AH, Taylor JL, Koretsky AP, Arai AE. Manganese enhanced magnetic resonance imaging of normal and ischemic canine heart. *Magn Reson Med* 2005;54(1):196-200.
27. Lin YJ, Koretsky AP. Manganese ion enhances T1-weighted MRI during brain activation: an approach to direct imaging of brain function. *Magn Reson Med* 1997;38(3):378-388.
28. Aoki I, Tanaka C, Takegami T, Ebisu T, Umeda M, Fukunaga M, Fukuda K, Silva AC, Koretsky AP, Naruse S. Dynamic activity-induced manganese-dependent contrast magnetic resonance imaging (DAIM MRI). *Magn Reson Med* 2002;48(6):927-933.
29. Krombach GA, Saeed M, Higgins CB, Novikov V, Wendland MF. Contrast-enhanced MR delineation of stunned myocardium with administration of MnCl₂ in rats. *Radiology* 2004;230(1):183-190.
30. Toft KG, Hustvedt SO, Grant D, Friisk GA, Skotland T. Metabolism of mangafodipir trisodium (MnDPDP), a new contrast medium for magnetic resonance imaging, in beagle dogs. *Eur J Drug Metab Pharmacokinet* 1997;22(1):65-72.
31. Waghorn B, Edwards T, Yang Y, Chuang KH, Yanasak N, Hu TC. Monitoring dynamic alterations in calcium homeostasis by T₁-weighted and T₁-mapping cardiac manganese-enhanced MRI in a murine myocardial infarction model. *NMR Biomed* 2008;21(10):1102-1111.
32. Clapham DE. Calcium signaling. *Cell* 2007;131(6):1047-1058.

33. Nordhoy W, Anthonsen HW, Bruvold M, Brurok H, Skarra S, Krane J, Jynge P. Intracellular manganese ions provide strong T1 relaxation in rat myocardium. *Magn Reson Med* 2004;52(3):506-514.
34. Bruvold M, Nordhoy W, Anthonsen HW, Brurok H, Jynge P. Manganese-calcium interactions with contrast media for cardiac magnetic resonance imaging: a study of manganese chloride supplemented with calcium gluconate in isolated Guinea pig hearts. *Invest Radiol* 2005;40(3):117-125.
35. Skjold A, Amundsen BH, Wiseth R, Stoylen A, Haraldseth O, Larsson HB, Jynge P. Manganese dipyridoxyl-diphosphate (MnDPDP) as a viability marker in patients with myocardial infarction. *J Magn Reson Imaging* 2007;26(3):720-727.
36. Hu TC, Pautler RG, MacGowan GA, Koretsky AP. Manganese-enhanced MRI of mouse heart during changes in inotropy. *Magn Reson Med* 2001;46(5):884-890.
37. Bremerich J, Saeed M, Arheden H, Higgins CB, Wendland MF. Normal and infarcted myocardium: differentiation with cellular uptake of manganese at MR imaging in a rat model. *Radiology* 2000;216(2):524-530.
38. Yankeelov TE, Gore JC. Dynamic Contrast Enhanced Magnetic Resonance Imaging in Oncology: Theory, Data Acquisition, Analysis, and Examples. *Curr Med Imaging Rev* 2009;3(2):91-107.
39. Tofts PS, Berkowitz B, Schnall MD. Quantitative analysis of dynamic Gd-DTPA enhancement in breast tumors using a permeability model. *Magn Reson Med* 1995;33(4):564-568.

40. Yankeelov TE, Gore JC. Dynamic Contrast Enhanced Magnetic Resonance Imaging in Oncology: Theory, Data Acquisition, Analysis, and Examples. *Curr Med Imaging Rev* 2009;3(2):91-107.
41. Donahue KM, Weisskoff RM, Parmelee DJ, Callahan RJ, Wilkinson RA, Mandeville JB, Rosen BR. Dynamic Gd-DTPA enhanced MRI measurement of tissue cell volume fraction. *Magn Reson Med* 1995;34(3):423-432.
42. Moran GR, Prato FS. Modeling tissue contrast agent concentration: a solution to the tissue homogeneity model using a simulated arterial input function. *Magn Reson Med* 2001;45(1):42-45.
43. Wendland MF. Applications of manganese-enhanced magnetic resonance imaging (MEMRI) to imaging of the heart. *NMR Biomed* 2004;17(8):581-594.
44. Gavin CE, Gunter KK, Gunter TE. Manganese and calcium transport in mitochondria: implications for manganese toxicity. *Neurotoxicology* 1999;20(2-3):445-453.
45. Sokoloff L, Reivich M, Kennedy C, Des Rosiers MH, Patlak CS, Pettigrew KD, Sakurada O, Shinohara M. The [¹⁴C]deoxyglucose method for the measurement of local cerebral glucose utilization: theory, procedure, and normal values in the conscious and anesthetized albino rat. *J Neurochem* 1977;28(5):897-916.
46. Silva AC, Lee JH, Aoki I, Koretsky AP. Manganese-enhanced magnetic resonance imaging (MEMRI): methodological and practical considerations. *NMR Biomed* 2004;17(8):532-543.
47. Brurok H, Schjott J, Berg K, Karlsson JO, Jynge P. Effects of manganese dipyridoxyl diphosphate, dipyridoxyl diphosphate--, and manganese chloride on

- cardiac function. An experimental study in the Langendorff perfused rat heart. *Invest Radiol* 1995;30(3):159-167.
48. Brurok H, Schjott J, Berg K, Karlsson JO, Jynge P. Manganese and the heart: acute cardiodepression and myocardial accumulation of manganese. *Acta Physiol Scand* 1997;159(1):33-40.
49. Nordhoy W, Anthonsen HW, Bruvold M, Jynge P, Krane J, Brurok H. Manganese ions as intracellular contrast agents: proton relaxation and calcium interactions in rat myocardium. *NMR Biomed* 2003;16(2):82-95.
50. Kim TH, Yang DH, Choi JW, Kim ST, Yoon JH, Shin JH, Seo JB, Gong GY, Lim TH. Manganese dipyradoxyl diphosphate (MnDPDP)-enhanced magnetic resonance imaging of acute reperfused myocardial injury in a cat model: part I: comparison with pathologic examination. *Invest Radiol* 2005;40(1):49-55.
51. MacGowan GA, Evans C, Hu TC, Debrah D, Mullet S, Chen HH, McTiernan CF, Stewart AF, Koretsky AP, Shroff SG. Troponin I protein kinase C phosphorylation sites and ventricular function. *Cardiovasc Res* 2004;63(2):245-255.
52. Li, W, O'Hara, T, Banerjee, S, Chaudhuri, P, Castel, L, Ye, A, Van Wagnoer, D, and Yu, X. Disrupted sarcolemmal nNOS signaling leads to increased L-type Ca^{2+} current and increased basal cardiac function in β -dystrobrevin knockout mice [abstract]. In: Anonymous. 2008.
53. Zhong J, Liu W, Yu X. Characterization of three-dimensional myocardial deformation in the mouse heart: an MR tagging study. *J Magn Reson Imaging* 2008;27(6):1263-1270.

54. Zhong J, Liu W, Yu X. Transmural myocardial strain in mouse: quantification of high-resolution MR tagging using harmonic phase (HARP) analysis. *Magn Reson Med* 2009;61(6):1368-1373.
55. Bers DM. Cardiac excitation-contraction coupling. *Nature* 2002;415(6868):198-205.
56. Bers DM. Cardiac excitation-contraction coupling. *Nature* 2002;415(6868):198-205.
57. Silva AC, Lee JH, Aoki I, Koretsky AP. Manganese-enhanced magnetic resonance imaging (MEMRI): methodological and practical considerations. *NMR Biomed* 2004;17(8):532-543.
58. Skjold A, Amundsen BH, Wiseth R, Stoylen A, Haraldseth O, Larsson HB, Jynge P. Manganese dipyridoxyl-diphosphate (MnDPDP) as a viability marker in patients with myocardial infarction. *J Magn Reson Imaging* 2007;26(3):720-727.
59. Li W, Griswold M, Yu X. Rapid T1 mapping of mouse myocardium with saturation recovery Look-Locker method. *Magn Reson Med* 2010;64(5):1296-1303.
60. Strijkers GJ, Mulder WJ, van Tilborg GA, Nicolay K. MRI contrast agents: current status and future perspectives. *Anticancer Agents Med Chem* 2007;7(3):291-305.
61. Edelman RR. Contrast-enhanced MR imaging of the heart: overview of the literature. *Radiology* 2004;232(3):653-668.
62. Saeed M, Wendland MF, Watzinger N, Akbari H, Higgins CB. MR contrast media for myocardial viability, microvascular integrity and perfusion. *Eur J Radiol* 2000;34(3):179-195.
63. Wagner A, Mahrholdt H, Sechtem U, Kim RJ, Judd RM. MR imaging of myocardial perfusion and viability. *Magn Reson Imaging Clin N Am* 2003;11(1):49-66.

64. Cron GO, Santyr G, Kelcz F. Accurate and rapid quantitative dynamic contrast-enhanced breast MR imaging using spoiled gradient-recalled echoes and bookend T(1) measurements. *Magn Reson Med* 1999;42(4):746-753.
65. Strijkers GJ, Mulder WJ, van Tilborg GA, Nicolay K. MRI contrast agents: current status and future perspectives. *Anticancer Agents Med Chem* 2007;7(3):291-305.
66. Koenig SH, Kellar KE. Theory of proton relaxation in solutions of magnetic nanoparticles, including the superparamagnetic size range. *Acad Radiol* 1996;3 Suppl 2:S273-S276.
67. Strich G, Hagan PL, Gerber KH, Slutsky RA. Tissue distribution and magnetic resonance spin lattice relaxation effects of gadolinium-DTPA. *Radiology* 1985;154(3):723-726.
68. Chuang KH, Koretsky A. Improved neuronal tract tracing using manganese enhanced magnetic resonance imaging with fast T(1) mapping. *Magn Reson Med* 2006;55(3):604-611.
69. Brookes JA, Redpath TW, Gilbert FJ, Murray AD, Staff RT. Accuracy of T1 measurement in dynamic contrast-enhanced breast MRI using two- and three-dimensional variable flip angle fast low-angle shot. *J Magn Reson Imaging* 1999;9(2):163-171.
70. Harrer JU, Parker GJ, Haroon HA, Buckley DL, Embelton K, Roberts C, Baleriaux D, Jackson A. Comparative study of methods for determining vascular permeability and blood volume in human gliomas. *J Magn Reson Imaging* 2004;20(5):748-757.

71. Parker GJ, Barker GJ, Tofts PS. Accurate multislice gradient echo T(1) measurement in the presence of non-ideal RF pulse shape and RF field nonuniformity. *Magn Reson Med* 2001;45(5):838-845.
72. Young IR, Bryant DJ, Payne JA. Variations in slice shape and absorption as artifacts in the determination of tissue parameters in NMR imaging. *Magn Reson Med* 1985;2(4):355-389.
73. Wang J, Qiu M, Kim H, Constable RT. T1 measurements incorporating flip angle calibration and correction in vivo. *J Magn Reson* 2006;182(2):283-292.
74. Crawley AP, Henkelman RM. A comparison of one-shot and recovery methods in T1 imaging. *Magn Reson Med* 1988;7(1):23-34.
75. Deichmann R, Hahn D, Haase A. Fast T1 mapping on a whole-body scanner. *Magn Reson Med* 1999;42(1):206-209.
76. Jakob PM, Hillenbrand CM, Wang T, Schultz G, Hahn D, Haase A. Rapid quantitative lung (1)H T(1) mapping. *J Magn Reson Imaging* 2001;14(6):795-799.
77. Steinhoff S, Zaitsev M, Zilles K, Shah NJ. Fast T(1) mapping with volume coverage. *Magn Reson Med* 2001;46(1):131-140.
78. Messroghli DR, Radjenovic A, Kozerke S, Higgins DM, Sivananthan MU, Ridgway JP. Modified Look-Locker inversion recovery (MOLLI) for high-resolution T1 mapping of the heart. *Magn Reson Med* 2004;52(1):141-146.
79. Messroghli DR, Walters K, Plein S, Sparrow P, Friedrich MG, Ridgway JP, Sivananthan MU. Myocardial T1 mapping: application to patients with acute and chronic myocardial infarction. *Magn Reson Med* 2007;58(1):34-40.

80. Waghorn B, Edwards T, Yang Y, Chuang KH, Yanasak N, Hu TC. Monitoring dynamic alterations in calcium homeostasis by T (1)-weighted and T (1)-mapping cardiac manganese-enhanced MRI in a murine myocardial infarction model. *NMR Biomed* 2008;21(10):1102-1111.
81. Chuang KH, Koretsky A. Improved neuronal tract tracing using manganese enhanced magnetic resonance imaging with fast T(1) mapping. *Magn Reson Med* 2006;55(3):604-611.
82. Karlsson M, Nordell B. Phantom and in vivo study of the Look-Locher T1 mapping method. *Magn Reson Imaging* 1999;17(10):1481-1488.
83. Steinhoff S, Zaitsev M, Zilles K, Shah NJ. Fast T(1) mapping with volume coverage. *Magn Reson Med* 2001;46(1):131-140.
84. Haacke EM BRTMVR. *Magnetic Resonance Imaging: Physical Principles and Sequence Design*. New York: Wiley; 1999.
85. Waghorn B, Edwards T, Yang Y, Chuang KH, Yanasak N, Hu TC. Monitoring dynamic alterations in calcium homeostasis by T (1)-weighted and T (1)-mapping cardiac manganese-enhanced MRI in a murine myocardial infarction model. *NMR Biomed* 2008;21(10):1102-1111.
86. Bland JM, Altman DG. Statistical methods for assessing agreement between two methods of clinical measurement. *Int J Nurs Stud* 2010;47(8):931-936.
87. Schneider JE, Cassidy PJ, Lygate C, Tyler DJ, Wiesmann F, Grieve SM, Hulbert K, Clarke K, Neubauer S. Fast, high-resolution in vivo cine magnetic resonance imaging in normal and failing mouse hearts on a vertical 11.7 T system. *J Magn Reson Imaging* 2003;18(6):691-701.

88. Dowell NG, Tofts PS. Fast, accurate, and precise mapping of the RF field in vivo using the 180 degrees signal null. *Magn Reson Med* 2007;58(3):622-630.
89. Cunningham CH, Pauly JM, Nayak KS. Saturated double-angle method for rapid B1+ mapping. *Magn Reson Med* 2006;55(6):1326-1333.
90. Deichmann R, Haase A. Quantification of T1 Values by SNAPSHOT-FLASH NMR imaging. *Journal of Magnetic Resonance* 1992;96:608-612.
91. Deichmann R. Fast high-resolution T1 mapping of the human brain. *Magn Reson Med* 2005;54(1):20-27.
92. Jivan A, Horsfield MA, Moody AR, Cherryman GR. Dynamic T1 measurement using snapshot-FLASH MRI. *J Magn Reson* 1997;127(1):65-72.
93. Schneider JE, Cassidy PJ, Lygate C, Tyler DJ, Wiesmann F, Grieve SM, Hulbert K, Clarke K, Neubauer S. Fast, high-resolution in vivo cine magnetic resonance imaging in normal and failing mouse hearts on a vertical 11.7 T system. *J Magn Reson Imaging* 2003;18(6):691-701.
94. Tafreshi NK, Kumar V, Morse DL, Gatenby RA. Molecular and functional imaging of breast cancer. *Cancer Control* 2010;17(3):143-155.
95. Fritz-Hansen T, Rostrup E, Larsson HB, Sondergaard L, Ring P, Henriksen O. Measurement of the arterial concentration of Gd-DTPA using MRI: a step toward quantitative perfusion imaging. *Magn Reson Med* 1996;36(2):225-231.
96. Larsson HB, Stubgaard M, Frederiksen JL, Jensen M, Henriksen O, Paulson OB. Quantitation of blood-brain barrier defect by magnetic resonance imaging and gadolinium-DTPA in patients with multiple sclerosis and brain tumors. *Magn Reson Med* 1990;16(1):117-131.

97. Simpson NE, He Z, Evelhoch JL. Deuterium NMR tissue perfusion measurements using the tracer uptake approach: I. Optimization of methods. *Magn Reson Med* 1999;42(1):42-52.
98. Weinmann HJ, Laniado M, Mutzel W. Pharmacokinetics of GdDTPA/dimeglumine after intravenous injection into healthy volunteers. *Physiol Chem Phys Med NMR* 1984;16(2):167-172.
99. Yankeelov TE, Cron GO, Addison CL, Wallace JC, Wilkins RC, Pappas BA, Santyr GE, Gore JC. Comparison of a reference region model with direct measurement of an AIF in the analysis of DCE-MRI data. *Magn Reson Med* 2007;57(2):353-361.
100. Pickup S, Zhou R, Glickson J. MRI estimation of the arterial input function in mice. *Acad Radiol* 2003;10(9):963-968.
101. Young IR, Bryant DJ, Payne JA. Variations in slice shape and absorption as artifacts in the determination of tissue parameters in NMR imaging. *Magn Reson Med* 1985;2(4):355-389.
102. Heilmann M, Walczak C, Vautier J, Dimicoli JL, Thomas CD, Lupu M, Mispelter J, Volk A. Simultaneous dynamic T1 and T2* measurement for AIF assessment combined with DCE MRI in a mouse tumor model. *MAGMA* 2007;20(4):193-203.
103. Lu H, Clingman C, Golay X, van Zijl PC. Determining the longitudinal relaxation time (T1) of blood at 3.0 Tesla. *Magn Reson Med* 2004;52(3):679-682.
104. Baruthio F, Guillard O, Arnaud J, Pierre F, Zawislak R. Determination of manganese in biological materials by electrothermal atomic absorption spectrometry: a review. *Clin Chem* 1988;34(2):227-234.

105. Tambalo S, Daducci A, Fiorini S, Boschi F, Mariani M, Marinone M, Sbarbati A, Marzola P. Experimental protocol for activation-induced manganese-enhanced MRI (AIM-MRI) based on quantitative determination of Mn content in rat brain by fast T1 mapping. *Magn Reson Med* 2009;62(4):1080-1084.
106. Giri S, Chung YC, Merchant A, Mihai G, Rajagopalan S, Raman SV, Simonetti OP. T2 quantification for improved detection of myocardial edema. *J Cardiovasc Magn Reson* 2009;11:56.
107. Higgins DM, Ridgway JP, Radjenovic A, Sivananthan UM, Smith MA. T1 measurement using a short acquisition period for quantitative cardiac applications. *Med Phys* 2005;32(6):1738-1746.
108. Gouya H, Vignaux O, Le RP, Chanson P, Bertherat J, Bertagna X, Legmann P. Rapidly reversible myocardial edema in patients with acromegaly: assessment with ultrafast T2 mapping in a single-breath-hold MRI sequence. *AJR Am J Roentgenol* 2008;190(6):1576-1582.
109. Donoho D. Compressed sensing. *IEEE Trans Inf Theory* 2006;52:1289-1306.
110. Lustig M, Donoho D, Pauly JM. Sparse MRI: The application of compressed sensing for rapid MR imaging. *Magn Reson Med* 2007;58(6):1182-1195.
111. Candes E.J., Wakin M.B. An introduction to compressive sampling. *IEEE SIGNAL PROC MAG* 2008;25:21-30.
112. Cukur T, Lustig M, Nishimura DG. Improving non-contrast-enhanced steady-state free precession angiography with compressed sensing. *Magn Reson Med* 2009;61(5):1122-1131.

113. Holland DJ, Malioutov DM, Blake A, Sederman AJ, Gladden LF. Reducing data acquisition times in phase-encoded velocity imaging using compressed sensing. *J Magn Reson* 2010;203(2):236-246.
114. Jung H, Sung K, Nayak KS, Kim EY, Ye JC. k-t FOCUSS: a general compressed sensing framework for high resolution dynamic MRI. *Magn Reson Med* 2009;61(1):103-116.
115. Gamper U, Boesiger P, Kozerke S. Compressed sensing in dynamic MRI. *Magn Reson Med* 2008;59(2):365-373.
116. Doneva M, Bornert P, Eggers H, Stehning C, Senegas J, Mertins A. Compressed sensing reconstruction for magnetic resonance parameter mapping. *Magn Reson Med* 2010.
117. Doneva M, Bornert P, Eggers H, Mertins A, Pauly J, Lustig M. Compressed sensing for chemical shift-based water-fat separation. *Magn Reson Med* 2010.
118. Tropp J, Gilbert A. Signal recovery from random measurement via orthogonal matching pursuit. *IEEE Trans Inf Theory* 2007;53:4655-4666.
119. Paulsen J, Bajaj VS, Pines A. Compressed sensing of remotely detected MRI velocimetry in microfluidics. *J Magn Reson* 2010;205(2):196-201.
120. Otazo R, Kim D, Axel L, Sodickson DK. Combination of compressed sensing and parallel imaging for highly accelerated first-pass cardiac perfusion MRI. *Magn Reson Med* 2010;64(3):767-776.
121. Liang D, Liu B, Wang J, Ying L. Accelerating SENSE using compressed sensing. *Magn Reson Med* 2009;62(6):1574-1584.

122. Ji JX, Zhao C, Lang T. Compressed sensing parallel magnetic resonance imaging. *Conf Proc IEEE Eng Med Biol Soc* 2008;2008:1671-1674.
123. Tofts PS, Brix G, Buckley DL, Evelhoch JL, Henderson E, Knopp MV, Larsson HB, Lee TY, Mayr NA, Parker GJ, Port RE, Taylor J, Weisskoff RM. Estimating kinetic parameters from dynamic contrast-enhanced T(1)-weighted MRI of a diffusable tracer: standardized quantities and symbols. *J Magn Reson Imaging* 1999;10(3):223-232.
124. Brasch R, Pham C, Shames D, Roberts T, van DK, van BN, Mann J, Ostrowitzki S, Melnyk O. Assessing tumor angiogenesis using macromolecular MR imaging contrast media. *J Magn Reson Imaging* 1997;7(1):68-74.
125. Patlak CS, Blasberg RG, Fenstermacher JD. Graphical evaluation of blood-to-brain transfer constants from multiple-time uptake data. *J Cereb Blood Flow Metab* 1983;3(1):1-7.
126. Seidler T, Hasenfuss G, Maier LS. Targeting altered calcium physiology in the heart: translational approaches to excitation, contraction, and transcription. *Physiology (Bethesda)* 2007;22:328-334.
127. Bassani JW, Bassani RA, Bers DM. Relaxation in rabbit and rat cardiac cells: species-dependent differences in cellular mechanisms. *J Physiol* 1994;476(2):279-293.
128. Varro A, Negretti N, Hester SB, Eisner DA. An estimate of the calcium content of the sarcoplasmic reticulum in rat ventricular myocytes. *Pflugers Arch* 1993;423(1-2):158-160.

129. Antoons G, Mubagwa K, Nevelsteen I, Sipido KR. Mechanisms underlying the frequency dependence of contraction and $[Ca^{2+}]_i$ transients in mouse ventricular myocytes. *J Physiol* 2002;543(Pt 3):889-898.
130. Pierdomenico SD, Di NM, Esposito AL, Di MR, Ballone E, Lapenna D, Cucurullo F. Prognostic value of different indices of blood pressure variability in hypertensive patients. *Am J Hypertens* 2009;22(8):842-847.